Recrystallization-induced oxygen isotope changes in inclusion-hosted water of speleothems – paleoclimatological implications

Attila Demény[1*], György Czuppon[1], Zoltán Kern[1], Szabolcs Leél-Őssy[2], Alexandra Németh[1], Máté Szabó[1], Mária Tóth[1], Chung-Che Wu[3], Chuan-Chou Shen[3], Mihály Molnár[4], Tibor Németh[1], Péter Németh[5], Mihály Óvári[6]

[1] Institute for Geological and Geochemical Research, RCAES, Hungarian Academy of Sciences, Budaörsi út 45, Budapest, H-1112, Hungary

[2] Department of Physical and Applied Geology, Eötvös Loránd University, Budapest, Pázmány Péter sétány. 1/C, H-1117, Hungary

[3] High-Precision Mass Spectrometry and Environment Change Laboratory (HISPEC), Department of Geosciences, National Taiwan University, Taipei 10617, Taiwan ROC

[4] Institute for Nuclear Research, Hungarian Academy of Sciences, Bem tér 18/c, Debrecen, H-4026, Hungary

[5] Institute of Materials and Environmental Chemistry, Research Centre for Natural Sciences, Hungarian Academy of Sciences, Magyar tudósok körútja 2., Budapest, H- 1117, Hungary

[6] Institute of Chemistry, Eötvös Loránd University, Budapest, Pázmány Péter sétány. 1/C, H-1117, Hungary

[*] Correspondence to demeny@geochem.hu

ABSTRACT

The issue of diagenetic alteration of carbonate deposits in caves (speleothems) has gained increasing importance in recent years, as this process has serious consequences for speleothem-based paleoclimate studies. In this study stable hydrogen and oxygen isotope data of water trapped in fluid inclusions were collected for recently forming stalagmites and flowstones in order to determine how dripwater compositions are reflected and preserved in the inclusion water compositions. Hydrogen isotope compositions were found to reflect dripwater values, whereas the oxygen isotope data were increasingly shifted from the local dripwater compositions with the time elapsed after deposition. The $\delta^{18}O$ data are correlated with X-Ray diffraction full width at half maximum values (related to crystal domain size and lattice strain), suggesting that the oxygen isotope shift is related to recrystallization of calcite. Transmission electron microscope analyses detected the presence of nanocrystalline (<50 nm) calcite, whose crystallization to coarser-grained calcite crystals (>200 nm) may have induced re-equilibration between the carbonate and the trapped inclusion water. The Ostwald ripening process provides an explanation for unexpectedly low oxygen isotope compositions in the inclusion water. The detected diagenetic alteration and its isotopic effects should be taken into consideration during sampling strategies and data evaluation as speleothems containing nanocrystalline calcite during their deposition are prone to late-stage oxygen isotope water-carbonate re-equilibration, which may shift the oxygen isotope composition of the inclusion water to more depleted values while the hydrogen isotope composition remains intact.

Keywords: speleothem, fluid inclusion, hydrogen and oxygen isotope compositions, diagenesis, Ostwald ripening

1. Introduction

Unlike sedimentary carbonate deposits, diagenetic alteration is relatively rarely detected in speleothems (cave-hosted carbonate deposits), as burial-related temperature elevation and influx of exotic fluids are not characteristic in cave environments. Most studies investigating the effects of diagenesis on speleothems have dealt with the transformation of primary aragonite to calcite associated with changes in the stable C and O isotope compositions and trace element contents (Martín-García et al, 2014; Zhang et al., 2014), or with infiltration of drip water into porous stalagmites, altering U-Th distribution and resulting in erroneous age dates (Scholz et al., 2014). Recrystallization in stalagmites has been studied by optical microscopy investigations that defined the main textural types and determined their evolution (Frisia, 1996; Frisia et al, 2000, 2010). Ostwald ripening has been proposed (Frisia et al., 2010) as a responsible mechanism for crystal-size coarsening, although purely on the basis of optical microscopy characteristics. Besides altering the carbonate's stable isotope and trace element compositions, diagenetic alteration and recrystallization may influence the isotopic compositions of inclusion-hosted water whose investigations became one of the most promisingly developing fields in speleothem research in the last decade (Vonhof et al., 2006; van Breukelen et al., 2008; Dublyansky and Spötl, 2009; Griffiths et al., 2010; Wainer et al., 2010; Rowe et al., 2012; Arienzo et al., 2013; Ayalon et al., 2013; Affolter et al., 2014). The stable H and O isotope ratios of inclusion-hosted water are thought to be preserved after the inclusion entrapment in speleothems (Harmon and Schwarz, 1981; Yonge, 1982), as they rarely suffer late-stage

alterations and isotope exchange at usual cave temperatures is negligible. In recent years the number of studies that presented inclusion-water compositions in agreement with expected values increased significantly, with limitations, however, in paleotemperature calculations (Wainer et al., 2010; Rowe et al., 2012). In this paper a set of speleothem deposits, including stalagmites and flowstones, with coupled δD-$\delta^{18}O$ (inclusion water) values were studied by optical microscopy, powder X-Ray diffraction (XRD) and transmission electron microscopy (TEM), in order to determine whether the observed oxygen isotopic shifts are related to textural, mineralogical or structural changes. This is the first study that reports speleothem crystallinity changes well beyond the resolution of optical microscopy analysis and demonstrates that these changes may be associated with alteration of stable oxygen-isotope composition of water trapped in fluid inclusions.

2. Samples and analytical methods

The studied speleothems formed in closed cave environments with constant ambient temperatures of around 10 ± 0.5 °C. After collection the samples were stored at room temperature (around 20 °C). A ~2 cm high, rather irregular stalagmite "hump" formed on the ground created in 1995, was collected in 2013 in the Csodabogyós ("CSB") Cave (W Hungary). The drip water's isotopic compositions are δD = –71.9 ± 1.1‰ and $\delta^{18}O$ = –10.35 ± 0.22‰, n=27. Two stalagmites of about 5 and 7 cm were collected from the Nehézút room ("NU") of the Baradla Cave (NE Hungary) where the drip water's compositions are δD = –66.2 ± 1.3‰ and $\delta^{18}O$ = –9.52 ± 0.18‰, n = 8. The third site is the travertine-like flowstone deposit formed within

the Béke Cave (Nagy-tufa, BNT) where two cores were drilled. One of the cores yielded meaningful U-Th dates (Shen et al., 2012) and was selected for detailed studies. The local drip water's isotopic compositions are $\delta D = -66.3 \pm 0.9‰$ and $\delta^{18}O = -9.47 \pm 0.17‰$, n = 19. Stream water at the deposit had practically identical isotope compositions ($\delta D = -65.7 \pm 1.3‰$ and $\delta^{18}O = -9.43 \pm 0.12‰$, n = 15) during the dripwater sampling period in 2013 and 2014.

Age-depth relations were established for all the samples on the base of collection dates, information on the beginning of deposition, lamina counting, position of ^{14}C "bomb peak" and U-Th dates. Detailed information on the locations, speleothems and dating methods are given in the Supplementary Material and in Demény et al. (2013).

Microscopic pictures were taken in crossed -polarised transmission light using a Nikon Eclipse E600 POL optical microscope. Thin sections polished on both sides were prepared with 0.3 mm thickness for fluid inclusion petrographic analyses using the optical microscope as above. For trace element concentration measurement about 10 mg of powdered sample was weighed into high purity 15 mL polypropylene centrifuge vials using an ultra-micro balance. The samples were dissolved in 12 mL 0.5 mol dm^{-3} nitric acid (Suprapure grade, E. Merck, Darmstadt, Germany). The analysis was carried out using an Element2 inductively coupled plasma sector field mass spectrometer (Thermo-Finnigan, Bremen, Germany). External calibration and internal standard solutions were prepared from multi and single element ICP standard stock solutions (E. Merck, Darmstadt, Germany).

Samples for X-ray diffraction (XRD) analyses were broken from the stalagmites and hand-powdered using an agate mortar and pestle in order to avoid structure distortion due to excessive grinding. XRD analysis was performed on a Philips PW-1730 diffractometer (PW-

1820/00 goniometer) equipped with a graphite monochromator using Cu-Kα radiation at 45 kV and 35 mA with 1^{o} divergence slit and 1^{o} receiving slit. Scanning rate was $0{,}05^{o}$ 2Θ per minute from 3° to 70°. Calcite (-104) reflection was also measured at 0.01 ^{o}2Θ/sec scanning speed (0.02 ^{o}2Θ step size, 2 sec scan time) in the 27.5 to 31.0 ^{o}2Θ range. Domain size was calculated using the well-known Scherrer equation (Scherrer, 1918) with Philips X'pert software from the parameters of the -104 peak with 0.01 width of standard profile. Based on replicate analyses, an average uncertainty of 25 Å can be attributed to the domain size data.

For transmission electron microscopy (TEM) study a few milligrams of the samples were crushed in ethanol and deposited onto a 3 mm lacey-carbon coated copper grid. Morphological and structural investigations of calcite samples were performed with a MORGAGNI 268D transmission electron microscope (100 kV accelerating voltage; W filament, top-entry; point-resolution = 0.5 nm).

Stable H and O isotope compositions of inclusion-hosted waters were determined by laser spectroscopic analyses. The method is based on the procedure described for fluorite-hosted water measurements (Czuppon et al., 2014) and modified for carbonate deposits (see Supplementary Material).

3. Results

3.1. Petrographic analyses

The textures of stalagmite samples are dominated by elongated columnar calcite with grain sizes of ~0.1-1 mm width and ~1-10 mm length (Supplementary Figs. S1 and S2). Mosaic texture was observed at the very base of the NU-1 stalagmite that was not sampled for isotope

analyses. No systematic crystal-size change was observed within the individual stalagmites, starting from the surface at the top toward the inner parts. The textural characteristics of travertine-like flowstone are more variable, covering several texture types (elongated columnar calcite, isometric clear calcite with cm-scale grain-crystal size, small dendritic crystals, pisolite-like structures; Supplementary Fig. S4) with straight or wavy layering of the growth laminae.

The appearance of fluid inclusions in the stalagmites (NU-1, NU-2 and CSB) and in the tufa deposit (BNT-2) are very similar to those described by earlier studies, although with texture-related differences in the different deposits. Both liquid and air-filled inclusions (see Scheidegger et al., 2010) are present. In the followings only the water-filled inclusions will be described as these were analysed for their H2O contents. In the studied stalagmites columnar calcites contain predominantly large (up to 0.5 mm in length), strongly elongated, frequently spindle-shaped inclusions (Fig. 1 A,B,E,G,H). The inclusions frequently show thorn- (Fig. 1F) or capillary-shaped (Fig. 1G,H) ends in the growth direction, similarly to the inclusion pictures presented by Meckler et al. (2015). Two-phase inclusions contain liquid and bubble (Fig. 1A,B,C,E) can also be detected. The stalagmite of the Csodabogyós Cave (sample CSB) is very inclusion-rich with numerous large inclusions oriented parallel with the growth direction (Fig. 1G). The inclusion -rich layers are alternating with inclusion-free or -poor ones (Fig. 1H), with very small inclusions in the latter. Opposite to the columnar calcite, the mosaic textured calcite detected at the oldest part of NU-1 stalagmite contain very few inclusions (Fig. 1D). Considering the generally diagenetic origin of mosaic texture (Frisia, 2015), this observation suggests that the inclusion content was partly lost during the re-crystallization process. This part of the stalagmite was not sampled for inclusion analysis.

The carbonate textures in the BNT-2 tufa deposit are significantly more variable than in the stalagmites, containing vuggy and dendritic textures beside different types of columnar calcite (open and closed, with varying crystal sizes). The columnar calcite contains abundant fluid inclusions with strongly elongated morphology, diffuse and irregular boundaries (Fig. 2A), that makes tracking the inclusions within the thin section difficult. The inclusion-rich layers are alternating with inclusion-poor ones that contain very small inclusions (Fig. 2B). Within the core vuggy calcite also formed that contains small, intracrystal inclusions (Fig. 2C). Dendritic calcite is also frequently observed with a scaffold-like texture (Frisia, 2015) of almost inclusion-free calcite rods (Fig. 2D). Trails of secondary inclusions formed during late-stage crack healing were not detected in the thin sections.

The petrographic characteristics of liquid inclusions are very similar to those described by Meckler et al. (2015) suggesting that most of the inclusions contain water trapped during the deposition of the carbonate. The inferred primary nature of inclusions gives credit to the isotope analyses of inclusion-hosted water.

3.2. Age determinations

Age estimations based on ^{14}C activity measurements (Supplementary Table S1) and U-Th dating (Supplementary Table S2) are described in the Supplementary material. The ^{14}C activity bomb peak of the year 1964 was detected in stalagmite NU-2, whose position proved that the lamination in these stalagmites represent annual layers. Lamina counting associated with ^{14}C activity measurements revealed that the CSB, NU-1 and NU-2 stalagmites' deposition started after 1996, 1976 and 1802. The U-Th ages obtained for the tufa drill core (BNT-2) indicate that

the tufa deposit was formed in the last ~4000 years, although an exact age-depth model could not be established due to the high detrital Th content in the BNT-2 samples. Further studies on the precise dating are planned, but it is beyond the scope of the present paper.

3.2. Chemical, mineralogical and isotopic compositions

Analyses of chemical compositions of stalagmites conducted for 47 samples from the NU-1, NU-2, BNT-2 and CSB speleothems yielded Mg and Sr concentrations below 3000 and 75 ppm, respectively (Supplementary Table S3). From a mineralogical point of view, the amount of detrital material was also negligible reflected by low Al and Si concentrations (below 3500 ppm). All the samples yielded characteristic calcite peaks in the powder X-Ray diffractograms without any sign of other carbonate types. The main calcite peak occurred at 29.39 ± 0.03 2Θ (corresponding to a *d*(104) value of 3.036 ± 0.003 Å) in all of the samples. However, the full width at half maximum (FWHM) values for the 2Θ=29.39 peak decrease with distance from the speleothems' surface at the top toward the base in all of the studied samples (Supplementary Table S4). Coherently scattering domain size values calculated using the Scherrer equation (Scherrer, 1918) increase with distance from the speleothems' surfaces starting from about 550 Å and yielded a maximum of about 740 Å in the older parts of the speleothem deposits (Supplementary Table S4). No clear relationship could be detected between textural types and domain sizes.

The inclusion-hosted water extracted from the speleothems yielded δD and $\delta^{18}O$ data close to the drip water compositions of the collection sites (Fig. 3, Supplementary Table S5). The 1σ standard deviations of the individual stalagmites' δD data (2.0-3.5 ‰) are in agreement with

the usually acceptable precisions, but the $\delta^{18}O$ scatter (1.1-1.5 ‰) is certainly higher than usual. Beside the large scatter, the $\delta^{18}O$ data are shifted to negative values compared to drip water compositions for the CSB, the NU-1 and the BNT-2 samples, while the average O isotope composition of the inclusion-hosted water of the NU-2 sample is identical to the local drip water's value. The δD values do not show any relationship with the distance from the speleothems' surfaces, whereas the $\delta^{18}O$ values display a clear negative shift with distance, and hence time elapsed after deposition (Fig. 4).

Figure 5 shows representative TEM images of the NU-2/4, BNT-2/31 and CSB-5 samples. Based on their crystal sizes and morphologies, two types of calcite – large fragments (>200 nm) and fine-grained (<50 nm) aggregates - were detected in the sample powders. Large fragments of well-developed calcite crystals are present in all of the studied sample powders, but they are the predominating constituent of BNT-2/31 sample, which represents the innermost part of the flowstone core (Fig. 5a). This form of calcite is several hundred nanometres in size, and is outlined by fairly straight edges. The other calcite type can be easily distinguished by TEM due to its fine crystal size, which usually does not exceed 50 nm. These calcite crystals occur as moderately elongated (BNT-2/31; Fig. 5b) or squat rhombohedra (NU-2/4; Figs. 5c and d) with rounded edges or partly straight edges (CSB-5; Figs. 5e and f). The spotty electron diffraction patterns (Fig. 5) and the observed lattice fringe images (*e.g.*, Fig. 5e insert) indicate that these nano-sized grains are single calcite crystals. They are aggregated and commonly occur at the border of the large calcite crystals. In general crystal sizes are smaller (20-30 nm on average) in samples collected from speleothem surfaces (CSB-5) than those sampled in the inner parts of the deposits (about 40-50 nm in NU-2/4 and especially in BNT-2/31).

4. Discussion

As shown in Fig. 3, at constant δD values the $\delta^{18}O$ data of inclusion-hosted waters are shifted from the local drip water compositions to ^{18}O-depleted values. This shift is related to distance from the surface, *i.e.*, the time elapsed after the deposition (Fig. 4). In theory, the observed isotope compositions could have been either primary or were produced by secondary alteration. In any case, the negative $\delta^{18}O$ shift can not be attributed to primary dripwater composition changes as the low $\delta^{18}O$ values are not associated with low δD values. The effect of post-deposition influx of external water can be excluded for the same reason.

If the $\delta^{18}O$ shifts were induced by *secondary, alteration-related processes*, the following options should be considered:

1) *Temperature change*. Based on experimentally determined calcite-water oxygen isotope-fractionation equations (O'Neil et al., 1969), every 1 °C increase in the 5-20 °C range would correspond to a –0.24‰ shift in the fractionation value. The 4-5‰ decrease in the water composition without any change in the calcite during a late-stage oxygen isotope exchange between the calcite and the inclusion-hosted water would require a temperature drop of 15-20 °C, which can be excluded both in the cave and during the sample storage.

2) *$CaCO_3$ mineral to calcite transition*. Aragonite-water oxygen-isotope fractionation is higher than that observed for calcite (Grossman and Ku, 1986; Lecuyer et al., 2012); thus, conversion of aragonite to calcite would lead to an increase in the inclusion-hosted water's O isotope composition, contrary to what observed. Formation of vaterite and its transformation to

calcite would not cause any significant isotopic change as the vaterite-water oxygen isotope fractionation is close to the calcite-water fractionation (Kluge and John, 2015). Hence this effect can also be excluded.

3) *Precipitation and transformation of amorphous calcium carbonate (ACC)*. Although direct measurements for the $CaCO_3$ system are not available, about 5‰ smaller carbonate-water oxygen isotope fractionation has been reported for amorphous Ca-Mg-carbonate than for crystalline dolomite (Schmidt et al., 2005). Assuming an analogous behaviour for calcium carbonate, the ACC-water oxygen isotope fractionation would be smaller than the calcite-water value. Transformation of ACC to calcite would result in increased fractionation, and as we consider small amount of water trapped in inclusions in a mass of host carbonate, the water composition should be shifted to lower $\delta^{18}O$ values. The major uncertainty of this model is that the ACC-water isotope fractionation has not been determined yet and that no sign of ACC has been detected. Nevertheless, it is important to note that the textures presented in Fig. 5 closely resemble the appearance of pseudomorphic nanocrystalline calcite aggregates formed after transformation of amorphous calcium carbonate ACC (Rodriguez-Navarro et al., 2015).

4) *Kinetic vs. equilibrium fractionation*. Rapid carbonate precipitation would enhance the effect of kinetic fractionation by preferential incorporation of more vigorously moving ^{16}O-rich carbonate ions. Independent information on the degree of kinetic fractionation has been provided by an experimental study (Dietzel et al., 2009) that showed several ‰ decrease in the calcite-water isotope fractionation with increasing precipitation rate (at a pH range of 8.3 to 9). If the isotope exchange is possible, the carbonate formed under kinetic conditions would approach equilibrium fractionation with the entrapped inclusion water at a later stage. Due to

calcite-water mass balance (very small amount of water trapped in a mass of calcite) the water composition would be shifted to negative direction to achieve the calcite-water equilibrium fractionation value. Such a difference in the kinetic vs. equilibrium fractionation may well explain the observed shifts in the inclusion-hosted water. Rapid precipitation may produce very fine grained carbonate, which is in accordance with the detection of nanocrystalline calcite.

These considerations have lead us to conclude that the observed negative $\delta^{18}O$ shift is related to a secondary alteration process, namely transformation of a relatively ^{16}O-enriched carbonate form to well crystallized calcite. Since the origin of the transforming carbonate is not known, it is called Precursor Calcium carbonate (PCC). The assumption of carbonate transformation process requires independent evidence that was provided by X-Ray diffraction analyses. As shown in Fig. 6, the negative $\delta^{18}O$ shift is associated with decreasing FWHM value, that means sharper XRD peaks due to larger crystallite size and/or less lattice imperfection. Although the XRD peak width values are determined by crystal domain size and lattice strain together, additional data indicate that significant and systematic lattice strain change is not expected in the studied speleothems.

Lattice strain is important if significant amounts of substituting ion (like Mg, Sr or Co) or organic material is incorporated in the calcite structure (Nielsen et al., 2013; Kim et al., 2014), or if the calcite was physically deformed as in the case of marbles (Chen et al., 2011). None of the above effects can be assumed for the studied speleothems in which the substituting ion concentrations are below 3000 ppm, organic concentrations are generally very low (below 2 mg l^{-1}) in the dripwaters of European caves even with quite different environments (Hartland et al., 2012) and no physical deformation occurred. Systematic variations of Mg incorporation within

the stalagmites should also be detected by shifts in the positions of the 104 peak in the XRD spectra (*d*104 value; Zhang et al., 2010). The *d*104 values (3.036 ± 0.003) indicate that the $MgCO_3$ content of the calcite is well below 1%, in accordance with the measured chemical compositions. Hence, although some microstrain may be present and the values obtained for crystallite size can be slightly underestimated, the available data suggest that the strain level is practically constant and the change in the FWHM data can be attributed solely to domain size variation. The crystallinity improvement and the domain size increase can be analogous to Ostwald ripening that may bring about crystal size increase in speleothems (Frisia et al., 2010). Ostwald ripening is a well-known process of crystallite size increase when small crystals merge by solid state diffusion or dissolution/reprecipitation to produce larger crystals in order to reduce the surface energy of the crystalline material. It should be noted here that there is a large scale difference between the optical microscopic textural features (mm scale) and the coherently scattering domains (<1 μm scale). Hence the two appearances of Ostwald ripening may not be directly compared.

Carbonate-water isotope exchange would either require fast oxygen diffusion or complete dissolution-reprecipitation of large amounts of calcite (relative to the concentration of inclusion-hosted water) in order to achieve equilibrium between the entrapped inclusion water and the host calcite. At the observed cave temperatures (~10 °C) oxygen diffusion is negligible in the calcite structure (Farver, 1994); thus diffusion-driven isotope exchange can be excluded. Instead, carbonate recrystallization can facilitate the carbonate-water isotope exchange, in which case the exchange rate would be dictated by the rate of recrystallization. This is supported by the comparison of FWHM values and $\delta^{18}O$ (inclusion water) changes. In order to

bring the inclusion-water compositions obtained for speleothems from distantly-separated sites to the same scale, the differences between $\delta^{18}O$ (inclusion water) values and drip water compositions at the given sites are plotted against distance from the deposits' surfaces. Figure 6 shows similar patterns for the FWHM and oxygen isotope changes, supporting the hypothesis that recrystallization induced and rate-limited the observed $\delta^{18}O$ (water) shift. In the absence of external fluids (as discussed above), recrystallization itself would not cause any change in the $\delta^{18}O$ values of the calcite, hence the observed shift must indicate an original disequilibrium between the carbonate and the inclusion-hosted water.

It is interesting to note that available literature data indicate that some of the differences in applications of fluid inclusion $\delta^{18}O$ analyses might be related to cave environments. The oxygen isotope compositions of inclusion waters of stalagmites from cold/temperate region caves could rarely be used for formation temperature calculations (Dennis et al., 2001; Wainer et al., 2010; Rowe et al., 2012), whereas inclusion waters of stalagmites from tropical caves have δD and $\delta^{18}O$ values close the local meteoric water compositions and yield appropriate formation temperatures (Van Breukelen et al., 2008; Griffiths et al., 2010; Affolter et al., 2014). In warm cave environments the higher temperature would promote formation of well crystallized calcite, whereas in cold caves hydrous carbonates, amorphous calcium carbonate or inhomogeneous calcite containing kinetically-affected nanocrystalline aggregates can form whose transformation can lead to isotopic alteration. These considerations imply that stalagmite $\delta^{18}O$ (inclusion water) data from cold/temperate regions should be evaluated with caution and that only the δD values might be used for paleoclimatic evaluations.

5. Conclusions

Stable hydrogen and oxygen isotope compositions of fluid inclusion water were determined for recently forming stalagmites and a flowstone sampled in Hungarian caves that cover the last 20 to 4000 years. The hydrogen isotope values reflect the local dripwater compositions, whereas only a part of the oxygen isotope compositions fit to the dripwater data. The $\delta^{18}O$ (inclusion water) values are consistently shifted to negative direction moving from the speleothem surface to the inner parts, *i.e.*, with the time elapsed after deposition. The isotopic shift is associated with crystallinity changes of the host calcite reflected by XRD peak width values (FWHM), suggesting that the recrystallization affected a carbonate form that was out of oxygen isotopic equilibrium at the time of precipitation. The isotopic disequilibrium can either be attributed to the formation of amorphous calcium carbonate that was later transformed to calcite, or precipitation of kinetically affected calcite. Beside well crystallized calcite grains (>200 nm), nanocrystalline calcite aggregates (with crystals <50 nm) were detected in the speleothems that can represent a product of mineral transformation or rapid precipitation, and whose recrystallization could have induced the calcite-water oxygen isotopic re-equilibration. Since the ultimate origin of the transforming carbonate is not known, it was called Precursor Calcium Carbonate (PCC) to include both amorphous carbonate and nanocrystalline calcite. The recrystallization-induced isotope exchange model is graphically presented in Fig. 7 that shows the formation of PCC with oxygen isotope compositions out of calcite-water equilibrium factionation, then recrystallization to coarser grained calcite due to Ostwald ripening. Re-

crystallization induced an approach to the calcite-water equilibrium fractionation and the water composition shift to negative $\delta^{18}O$ values. Literature data indicate that fluid inclusion $\delta^{18}O$ data of speleothems from cold/temperate caves might be more frequently affected by late-stage processes than those from tropical caves due to the higher chance of well crystallized calcite formation at higher temperatures. The present results indicate that $\delta^{18}O$ (inclusion water) data from cold/temperate caves should be interpreted with caution.

Acknowledgements

Yuri Dublyansky and Hubert Vonhof are gratefully thanked for providing comparisons between samples and for their open discussions. The authors are deeply indebted to Henry M. Lieberman for polishing the paper's English. Lively discussions with Prof. Martin Dietzel helped clarify our ideas. This research was supported by the National Office for Research and Technology of Hungary (GVOP-3.2.1-2004-04-0235/3.0), the Hungarian Scientific Research Fund (OTKA CK 80661 and OTKA NK 101664) and the “Momentum-Lendület” program of the Hungarian Academy of Sciences (LP2012-27/2012). U-Th dating was supported by Taiwan ROC MOST and NTU grants (103-2119-M-002-022, 101R7625). This is contribution No. 31 of the 2ka Palaeoclimatology Research Group.

References

Affolter, S., Fleitmann, D., Leuenberger, M., 2014. New online method for water isotope analysis of speleothem fluid inclusions using laser absorption spectroscopy (WS-CRDS). Climate of the Past 10, 1291-1304.

Arienzo, M.M., Swart, P.K., Vonhof, H.B., 2013. Measurement of $\delta^{18}O$ and $\delta^{2}H$ values of fluid inclusion water in speleothems using cavity ring-down spectroscopy compared with isotope ratio mass spectrometry. Rapid Communications in Mass Spectrometry 27, 2616-2624.

Ayalon, A., Bar-Matthews, M., Frumkin. A., Matthews, A., 2013. Last glacial warm events on Mount Hermon: the southern extension of the Alpine karst range of the east Mediterranean. Quaternary Science Reviews 59, 43-56.

Chen, K., Kunz, M., Tamura, N., Wenk, H.-R., 2011. Deformation twinning and residual stress in calcite studied with synchrotron polychromatic X-ray microdiffraction. Physics and Chemistry of Minerals 38, 491-500.

Czuppon, Gy., Ramsay, R.R., Özgenc, I., Demény, A., Gwalani, L.G., Rogers, K., Eves, A., Papp, L., Palcsu, L., Berkesi, M., Downes, P.J., 2014. Stable (H, O, C) and noble-gas (He and Ar) isotopic compositions from calcite and fluorite in the Speewah Dome, Kimberley Region, Western Australia: implications for the conditions of crystallization and evidence for the influence of crustal-mantle fluid mixing. Mineralogy and Petrology 108, 759-775.

Demény, A., Czuppon, Gy., Siklósy, Z., Leél-Őssy, Sz., Lin, K., Shen, C-C., Gulyás, K., 2013. Mid-Holocene climate conditions and moisture source variations based on stable H, C and O

isotope compositions of speleothems in Hungary. Quaternary International. 293. 150-156.

Dennis, P. F., Rowe, P. J., Atkinson, T. C., 2001. The recovery and isotopic measurement of water from fluid inclusions in speleothems. Geochimica et Cosmochiica. Acta 65, 871-884.

Dietzel M., Tang, J., Leis, A., Köhler, S., 2009. Stable isotopic fractionation during inorganic calcite precipitation – Effects of temperature, precipitation rate and pH. Chemical Geology 268, 107-115.

Dublyansky, Y., Spötl, C., 2009. Hydrogen and oxygen isotopes of water from inclusions in minerals: design of a new crushing system and on-line CF-IRMS analysis. Rapid Communications in Mass Spectrometry. 23, 2605-2613.

Farver, J.R, 1994. Oxygen self-diffusion in calcite: dependence on temperature and water fugacity. Earth and Planetary Science Leters. 121, 575–587.

Frisia, S., Borsato, A.. 2010. Karst. In: Alonso-Zarza, A.M., Tanner, L.H. (Eds.), Developments in Sedimentology. Elsevier, pp. 269-318.

Frisia, S., 1996. Petrographic evidences of diagenesis in speleothems: some examples. Speleochronos 7, 21-30.

Frisia, S., 2015. Microstratigraphic logging of calcite fabrics in speleothems as tool for palaeoclimate studies. International Journal of Speleology 44, 1-16.

Frisia, S., Borsato, A., Fairchild, I.J., McDermott, F. 2000. Calcite fabrics, growth mechanisms, and environments of formation in speleothems from the Italian Alps and southwestern Ireland. Journal of Sedimentary Research 70, 1183-1196.

Griffiths, M.L., Drysdale, R. N., Vonhof, H.B., Gagan, M.K., Zhao, J-x., Ayliffe, L.K., Hantoro, W.S., Hellstrom, J.C., Cartwright, I., Frisia, S., Suwargadi, B.W., 2010. Younger Dryas-Holocene temperature and rainfall history of southern Indonesia from $\delta^{18}O$ in speleothem calcite and fluid inclusions. Earth and Planetary Science Letters 295, 30-36.

Grossman, E. L., Ku, T. L., 1986. Oxygen and carbon isotope fractionation in biogenic aragonite: temperature effects. Chemical Geology (Isotope Geoscience Section) 59, 59-74.

Harmon, R. S., Schwarcz, H.P., 1981. Changes in ^{2}H and ^{18}O enrichment of meteoric water and Pleistocene glaciations. Nature 290, 125-128.

Hartland, A., Fairchild, I.J. Lead, J.R., Borsato, A., Baker, A., Frisia, S., Baalousha, M., 2012 From soil to cave: transport of trace metals by natural organic matter in karst dripwaters. Chemical Geology, 304-305, 68-82.

Ihli, J., Wong, W.C., Noel, E.H., Kim, Y.Y., Kulak, A.N., Christenson, H.K., Duer, M.J., Meldrum, F.C., 2014. Dehydration and crystallization of amorphous calcium carbonate in solution and in air. Nature Communications 5, 3169.

Kim, Y.Y. Schenk, A.S. Ihli, J. Kulak, A.N. Hetherington, N.B.J. Tang, C.C. Schmahl, W.W. Griesshaber, E. Hyett, G. Meldrum, F.C., 2014. A critical analysis of calcium carbonate mesocrystals. Nat. Commun. 5, 4341.

Kluge, T., John, C.M., 2015. Technical Note: A simple method for vaterite precipitation for isotopic studies: implications for bulk and clumped isotope analysis. Biogeosciences, 12, 3289-3299.

Lecuyer, C., Hutzler, A., Amiot, R., Daux, V., Grosheny, D., Otero, O., Martineau, F., Fourel, F., Balter, V., Reynard, B., 2012. Carbon and oxygen isotope fractionations between

aragonite and calcite of shells from modern molluscs. Chemical Geology 332–333, 92-101.

Martín-García, R., Alonso-Zarza, A. M., Martín-Pérez, A., Schröder-Ritzrau, A., Ludwig, T., 2014. Relationships between colour and diagenesis in the aragonite-calcite speleothems in Basajaún Etxea cave, Spain. Sedimentary Geology 312, 63-75.

Meckler, A. N., Affolter, S., Dublyansky, Y. V., Kruger, Y., Vogel, N., Bernasconi, S. M., Frenz, M., Kipfer, R., Leuenberger, M., Spotl, C., Carolin, S., Cobb, K. M., Moerman, J., Adkins, J. F., Fleitmann, D., 2015. Glacial-interglacial temperature change in the tropical West Pacific: a comparison of stalagmite-based paleo-thermometers. Quaternary Science Reviews 127, 90-116.

Nielsen, L. C., De Yoreo, J. J., DePaolo, D. J., 2013. General model for calcite growth kinetics in the presence of impurity ions. Geochimica et Cosmochimica Acta 115, 100-114.

O'Neil, J. R., Clayton, R., Mayeda, T., 1969. Oxygen isotopic fractionation in divalent metal carbonates. The Journal of Chemical Physics 51, 5547-5558.

Rodriguez-Navarro, C., Kudlacz, K., Cizer, Ö., Ruiz-Agudo, E., 2015. Formation of amorphous calcium carbonate and its transformation into mesostructured calcite. CrystEngComm 17, 58-72.

Rowe, P.J., Mason, J.E., Andrews, J.E., Marca, A.D., Thomas, L., van Calsteren, P., Jex, C.N., Vonhof, H. B., Al-Omari, S., 2012. Speleothem isotopic evidence of winter rainfall variability in northeast Turkey between 77 and 6ka. Quaternary Science Reviews 45, 60-72.

Scheidegger, Y., Baur, H., Brennwald, M.S., Fleitmann, D., Wieler, R., Kipfer, R., 2010. Accurate analysis of noble gas concentrations in small water samples and its application to fluid inclusions in stalagmites. Chemical Geology 272, 31-39.

Scherrer, P., 1918. Bestimmung der Grösse und der inneren Struktur von Kolloidteilchen mittels Röntgenstrahlen. Nachrichten von der Gesellschaft der Wissenschaften zu Göttingen 26, 98-100.

Schmidt, M., Xeflide, S., Botz, R., Mann, S., 2005. Oxygen isotope fractionation during synthesis of CaMg-carbonate and implications for sedimentary dolomite formation. Geochimica et Cosmochimica Acta 69, 4665-4674.

Scholz, D., Tolzmann, J., Hoffmann, D. L., Jochum, K. P., Spötl, C., Riechelmann, D. F. C., 2014. Diagenesis of speleothems and its effect on the accuracy of ^{230}Th/U-ages. Chemical Geology 387, 74-86.

Shen, C.-C., Wu C.-C., Cheng H., Edwards R. L., Hsieh Y.-T., Gallet S., Chang C.-C., Li T.-Y., Lam D. D., Kano A., Hori M., Spötl C., 2012. High-precision and high-resolution carbonate ^{230}Th dating by MC-ICP-MS with SEM protocols. Geochimica et Cosmochimica Acta 99, 71-86.

van Breukelen, M. R., Vonhof, H. B., Hellstrom, J. C., Wester, W. C. G., Kroon, D., 2008. Fossil dripwater in stalagmites reveals Holocene temperature and rainfall variation in Amazonia. Earth and Planetary Science Letters 275, 54-60.

Vonhof, H. B., van Breukelen, M. R., Postma, O., Rowe, P. J., Atkinson, T. C., Kroon, D., 2006. A continuous-flow crushing device for on-line δ^2H analysis of fluid inclusion water in speleothems. Rapid Communications in Mass Spectrometry 20, 2553-2558.

Wainer, K., Genty, D., Blamart, D., Daëron, M., Bar-Matthews, M., Vonhof, H., Dublyansky, Y., Pons-Branchu, E., Thomas, L., van Calsteren, P., Quinif, Y., Caillon, N., 2011. Speleothem record of the last 180 ka in Villars cave (SW France): Investigation of a large $\delta^{18}O$ shift between MIS6 and MIS5. Quaternary Science Reviews. 30, 130-146.

Yonge, C. J., 1982. Stable Isotope Studies of Water Extracted from Speleothems. PhD thesis, McMaster University, Hamilton, ON, Canada.

Zhang, F., Xu, H., Konishi, H., Roden, E. E., 2010. A relationship between d_{104} value and composition in the calcite-disordered dolomite solid-solution series. American Mineralogist 95, 1650-1656.

Zhang, H., Cai, Y., Tana, L., Qina, S., Ana, Z., 2014. Stable isotope composition alteration produced by the aragonite-to-calcite transformation in speleothems and implications for paleoclimate reconstructions. Sedimentary Geology 309, 1-14.

Figures

Fig. 1. Optical microphotographs of stalagmites taken in transmitted light with crossed Nicols. Horizontal black bars show the length of 0.1 mm. Arrows indicate growth direction. A) Top of the NU-1 stalagmite close to the outer surface. B) and C) Inclusions in columnar calcite close to the base of the NU-1 stalagmite. D. Inclusions in mosaic calcite at the base of the NU-1 stalagmite. E) Spindle-shaped liquid inclusions (note the bubble-containing two-phase inclusion) at the top of the NU-2 stalagmite. F) Thorn-shaped liquid inclusions close to the base of the NU-2 stalagmite. G) and H) Liquid inclusions within the CSB stalagmite. Note that the inclusion rich layers are separated by inclusion-free (G, middle) or inclusion-poor (H, middle) microlayers.

Fig. 2. Optical microphotographs of the BNT-2 tufa drill core taken in transmitted light with crossed Nicols. Horizontal black bars show the length of 0.1 mm. Arrows indicate growth direction. A) Elongated inclusions in columnar calcite. B) Inclusion-poor layers in columnar calcite. C) Vuggy calcite with clouds of small inclusions in the crystals' interiors. D) Inclusion-poor dendritic calcite.

Fig. 3. Stable hydrogen and oxygen isotope compositions (in ‰ relative to V-SMOW) of drip waters and inclusion-hosted waters. GMWL: Global Meteoric Water Line. Drip water compositions: large yellow square – Baradla and the Béke caves (indistinguishable at this scale), large blue square – drip waters in the Csodabogyós Cave. Inclusion-hosted water compositions: yellow circles – NU-1 stalagmite, yellow squares – NU-2 stalagmite, blue circles: CSB stalagmite, stars – BNT-2 flowstone core.

Fig. 4 Stable hydrogen and oxygen isotope compositions (in ‰ relative to V-SMOW) of drip waters (large squares) and inclusion-hosted waters as a function of distance from the surface. Legend as in Fig. 1.

Fig. 5. Transmission electron microscopy images and electron diffraction patterns of powdered samples of flowstone (a-c: sample BNT-2/31) and stalagmites (d-f: sample NU-2/4; g-i: sample CSB-5). The electron diffraction patterns correspond to calcite nanocrystalline aggregates (white indices).

Fig. 6. $\delta^{18}O$ (inclusion water) changes relative to drip water compositions and Full Width at Half Maximum (FWHM) values as a function of distance from speleothem surface.

Fig. 7. Schematic model (based on a recently published review by Ihli et al., 2014) of ACC and/or nanocrystalline calcite formation (including both as Precursor Calcium Carbonate – PCC) along with coarser grained calcite precipitation (a) followed by transformation of ACC and nanocrystalline carbonate to well crystallized calcite and it's oxygen isotopic equilibration with the water entrapped in fluid inclusions (b).

Figure 1

Click here to download high resolution image

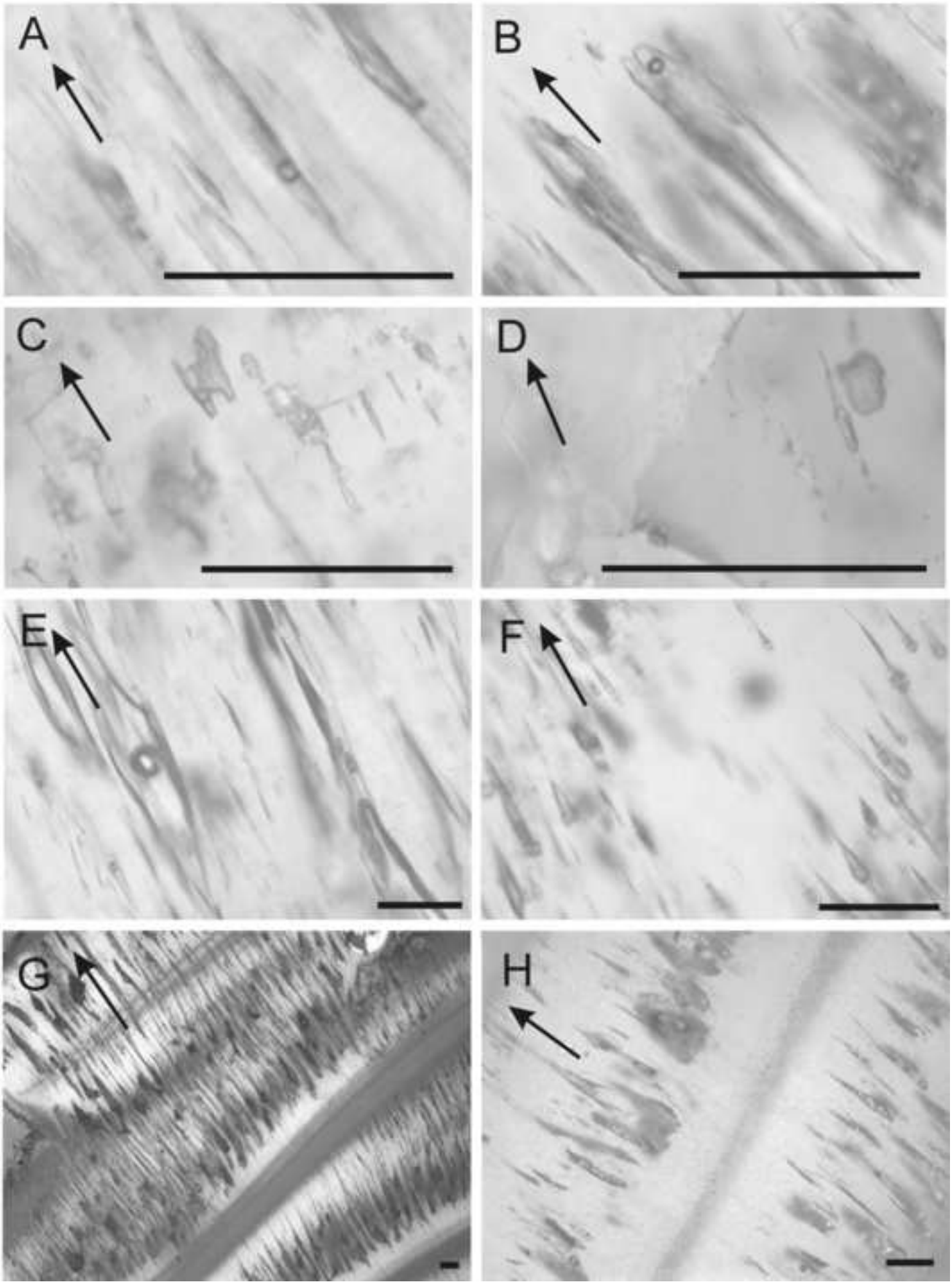

Figure 2

Click here to download high resolution image

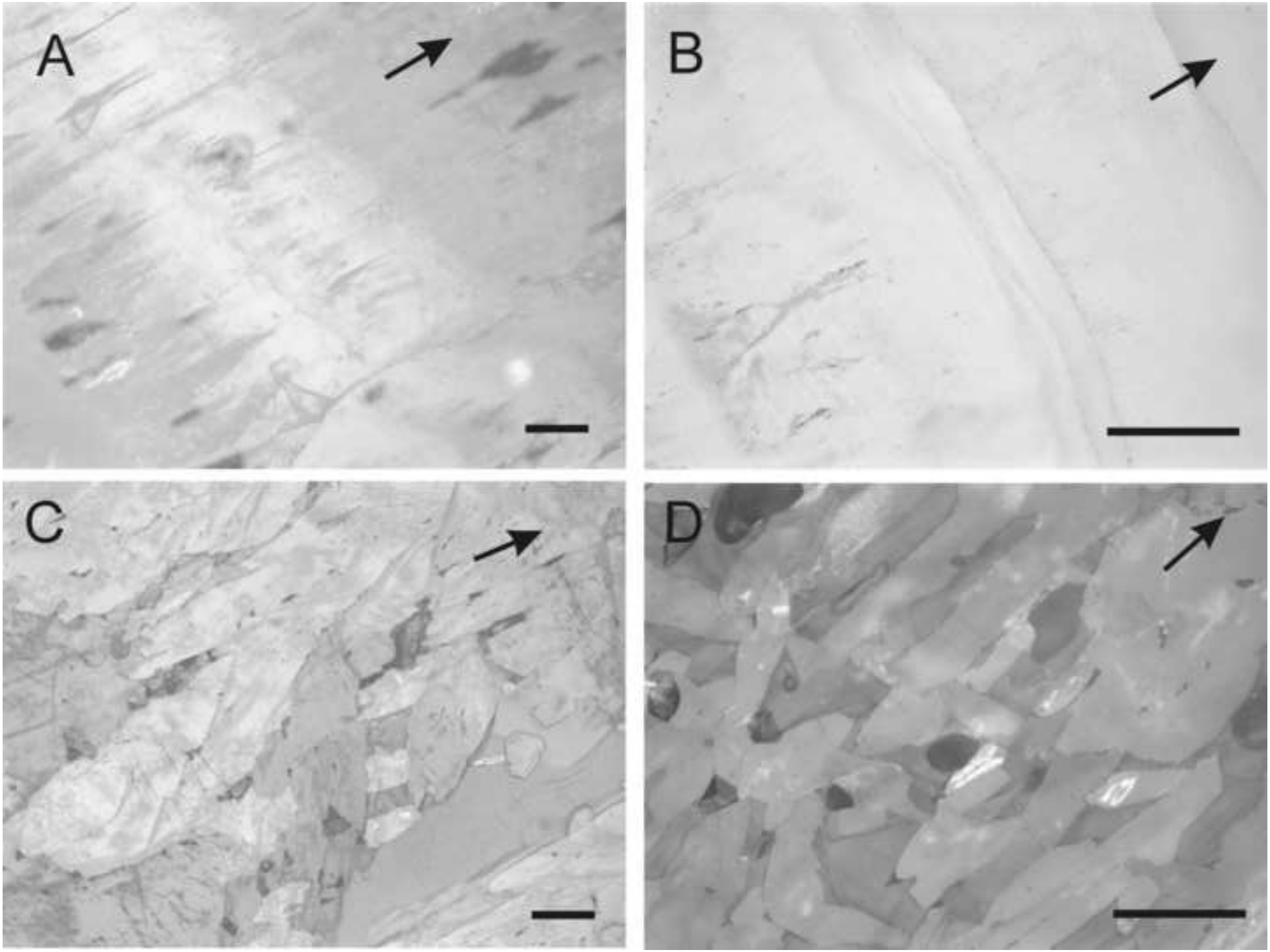

Figure 3

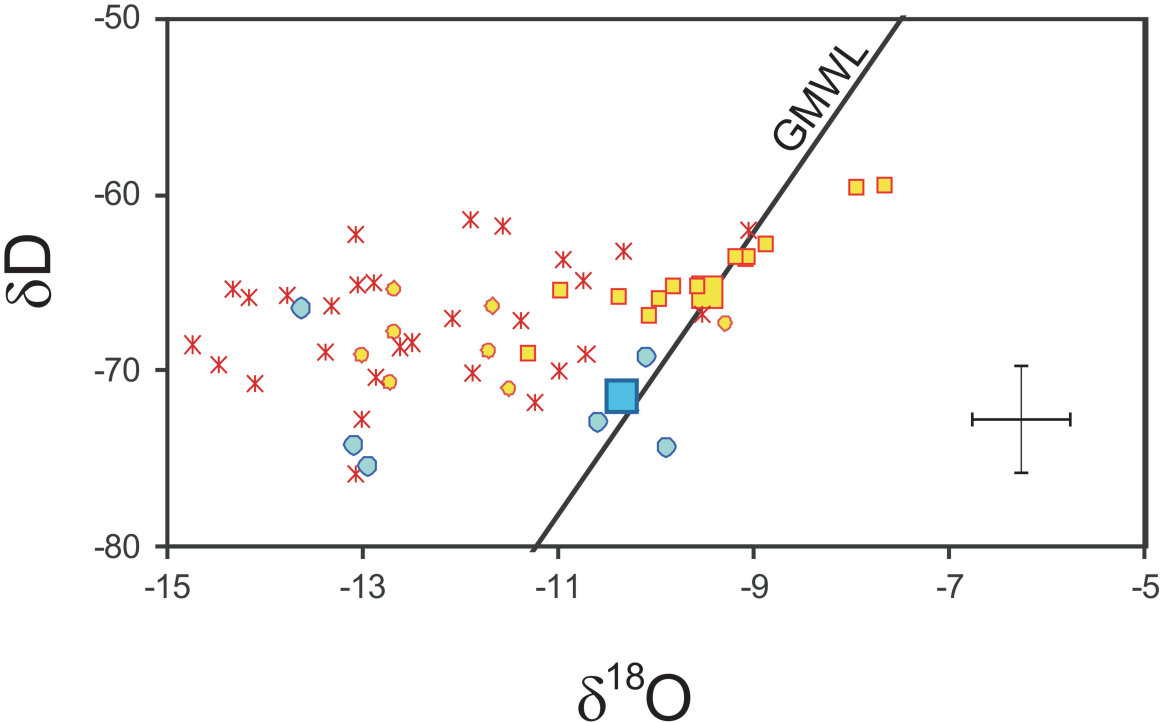

Figure 4

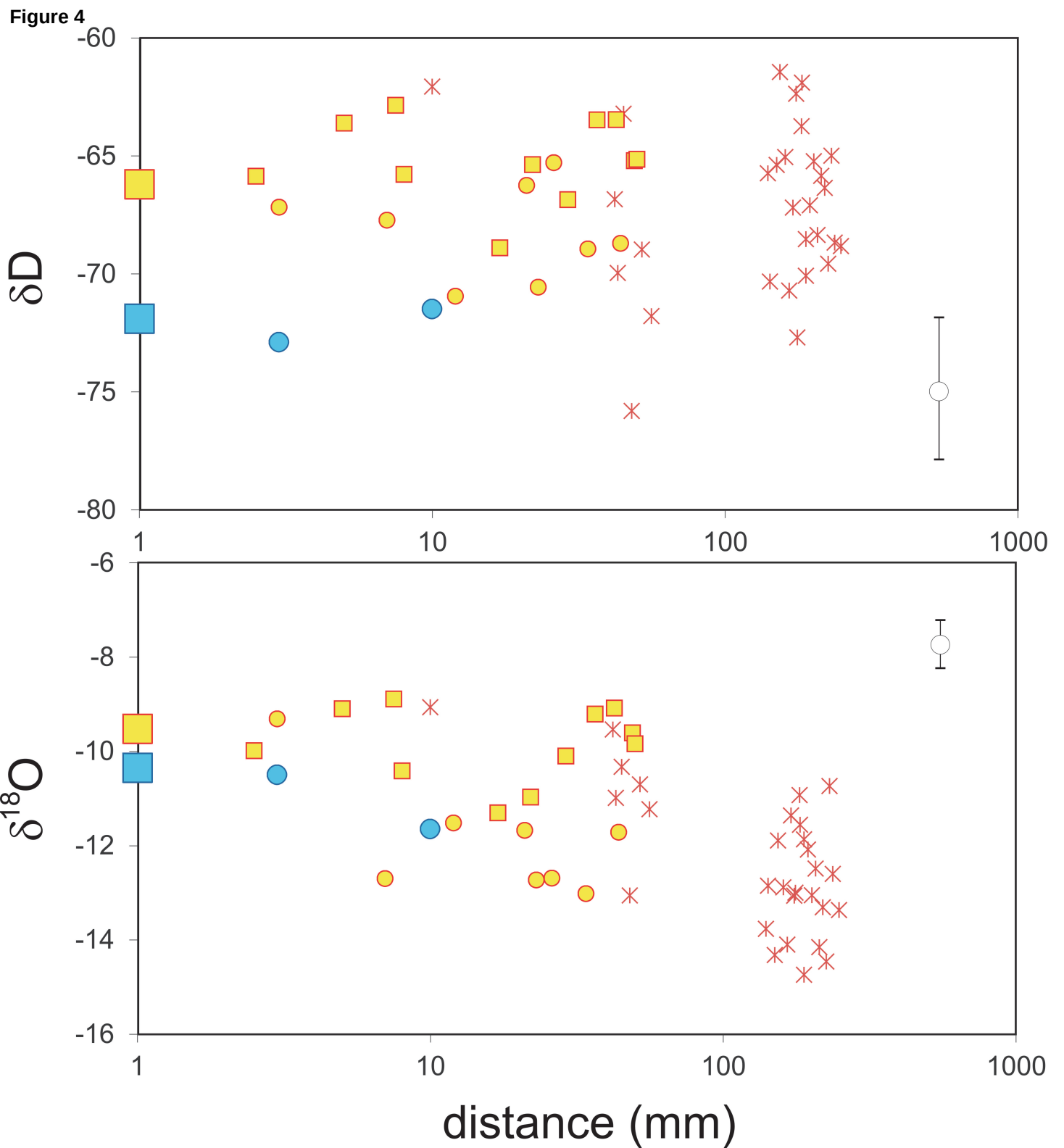

Figure 5

Click here to download high resolution image

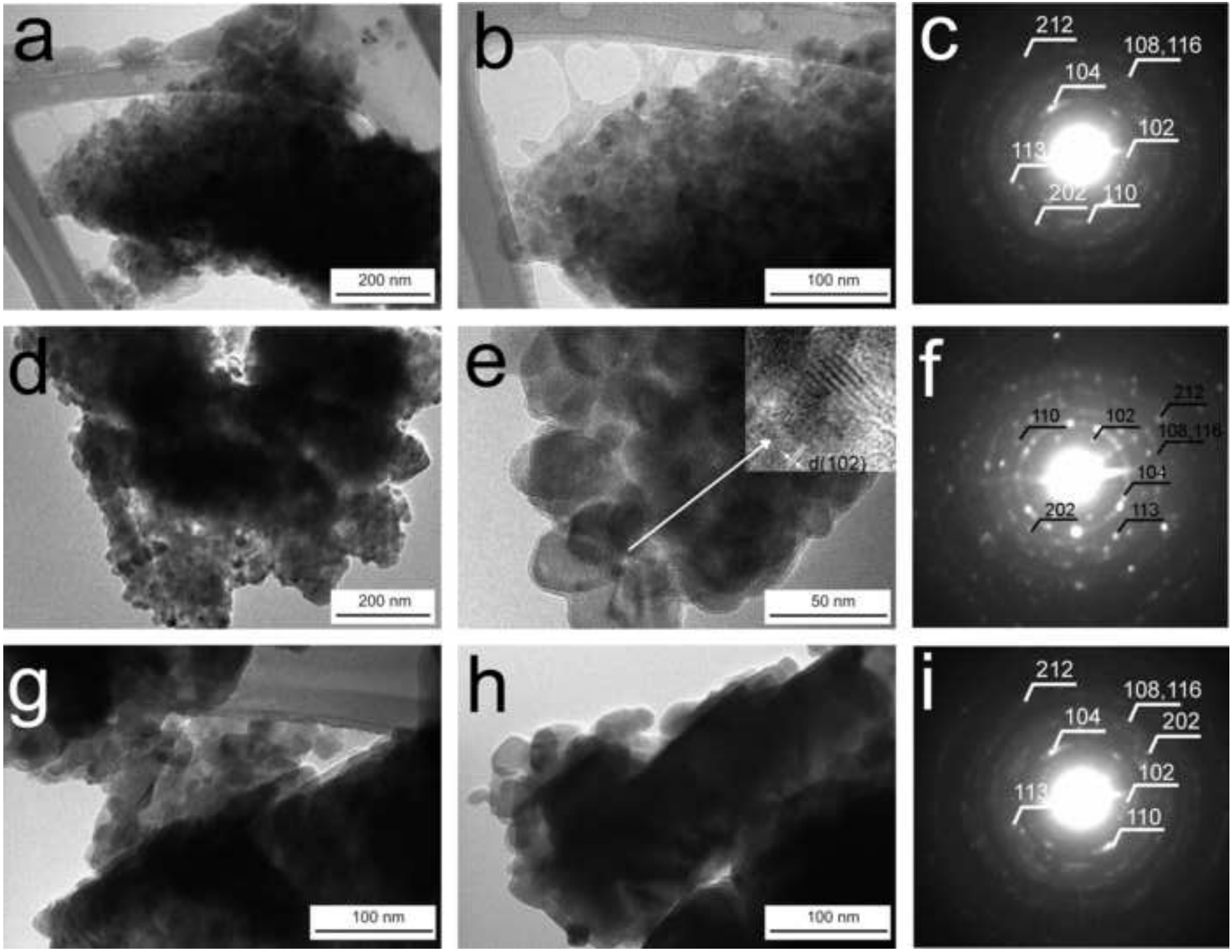

Figure 6

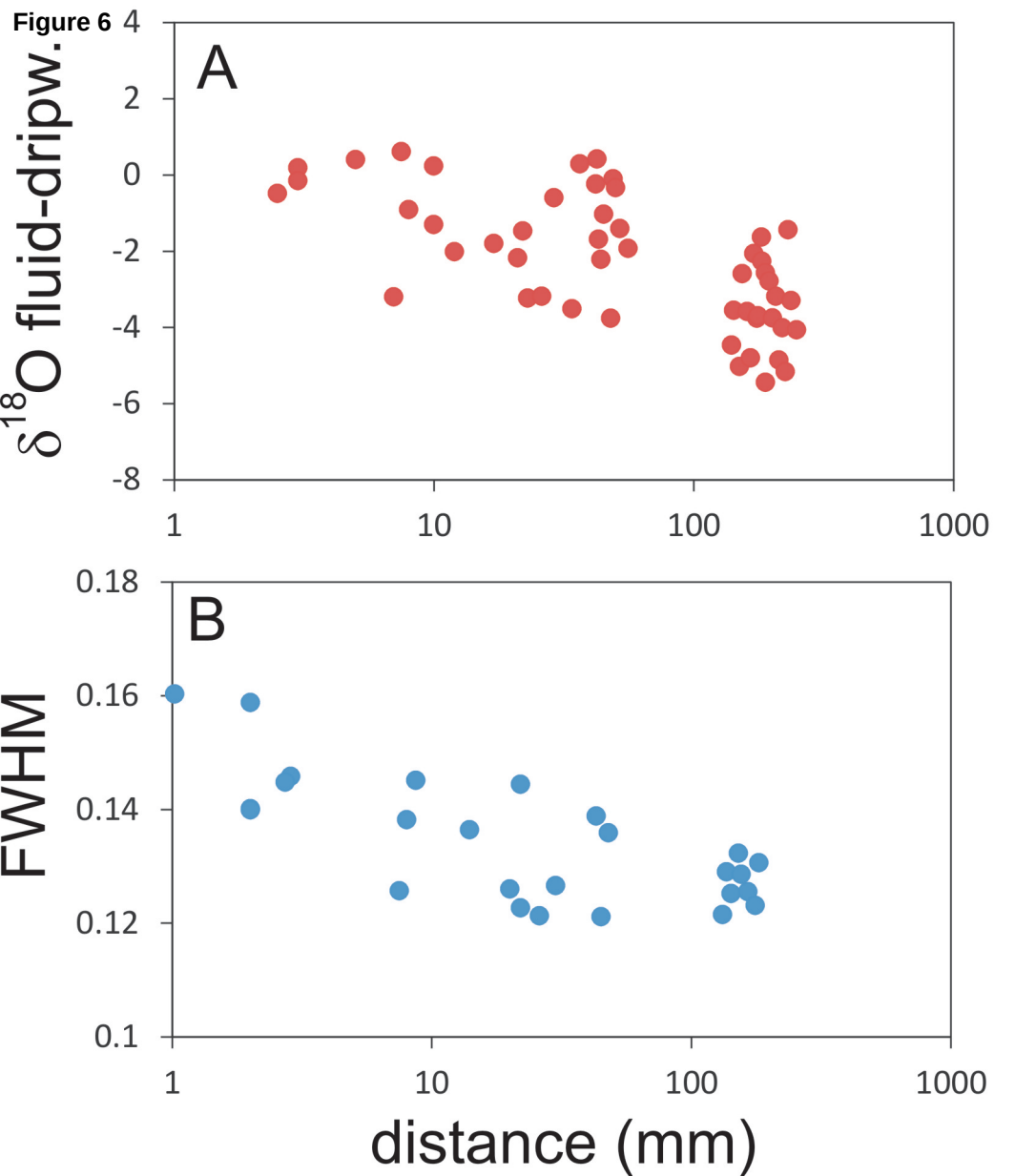
A
B
δ18O fluid-dripw.
FWHM
distance (mm)
4
2
0
-2
-4
-6
-8
0.18
0.16
0.14
0.12
0.1
1
10
100
1000

Figure 2

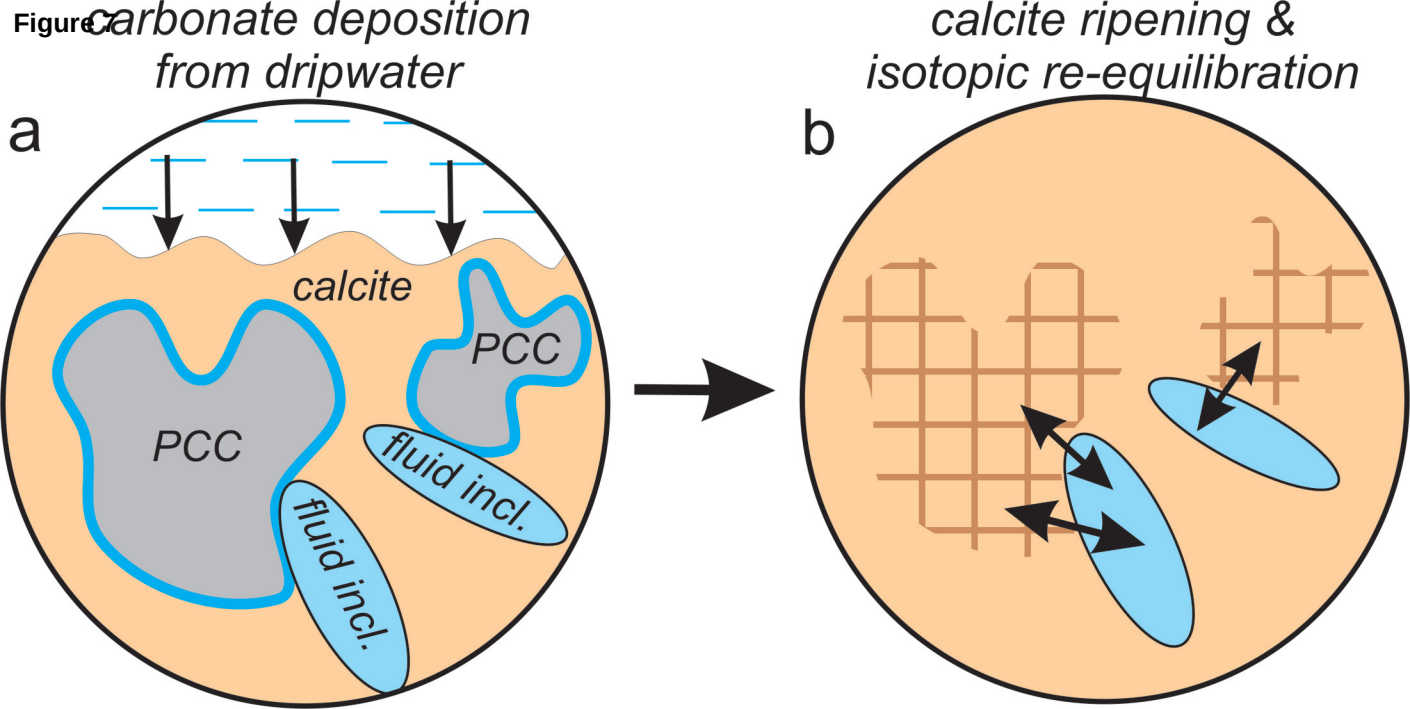
carbonate deposition
from dripwater
calcite ripening &
isotopic re-equilibration
a
b
calcite
PCC
PCC
fluid incl.
fluid incl.

Recrystallization-induced oxygen isotope changes in inclusion-hosted water of speleothems – paleoclimatological implications

Attila Demény[1*], György Czuppon[1], Zoltán Kern[1], Szabolcs Leél-Őssy[2], Alexandra Németh[1], Máté Szabó[1], Mária Tóth[1], Chung-Che Wu[3], Chuan-Chou Shen[3], Mihály Molnár[4], Tibor Németh[1], Péter Németh[5], Mihály Óvári[6]

Supplementary Material

Contents

I. Cave site descriptions

The studied caves are located in the northeastern (Baradla and Béke Caves) and the western (Csodabogyós Cave) parts of Hungary.

Baradla Cave

N48°28´ E020°30´

The cave is located in the north-eastern part of Hungary (in the Gömör-Torna Karst) at the Hungaria-Slovakia border. The bigger part (20.5 km) is in Hungary, the shorter part (5.5 km) belongs to Slovakia (Domica Cave). The area of this karstic cave belongs to the territory of Aggtelek National Park, and (together with other caves in this region) is the part of the UNESCO World Heritage. The cave entrance is situated in a forested area at 350 m a.s.l., the main passages are almost horizontal, ubiquitously characterized by big corridors (up to 10 m wide and 15 m high) and well decorated with large dripstones. The cave formed in lagoon facies of the Wetterstein Limestone of the Triassic (Ladinian) age. The cave temperature was 10.1 ±0.5 °C in 2013-2014 (spot measurements, n=8) that corresponds to the mean annual temperature at the surface. The annual precipitation in the area in the period of 1961 to 2015 ranged from 400 to 1000 mm with an average of 630 mm (source: Hungarian Meteorological Service), dominated by rain falling in May and June. Two samples were taken from the Aggtelek part of the cave, ca. 1100 m from the main entrance. The collection site is called „Nehéz út” ("Hard Way"), abbreviated here as NU. This point is under the highest part of the hill above the cave. The thickness of the overlying rocks is about 150 m.

Béke Cave

N 48° 29', E 20° 31'

This 7 km-long cave is situated in the north-eastern part of Hungary (in the Gömör-Torna Karst), only 1-2 km from the Baradla Cave. The main entrance is situated at about 250 m a.s.l. The water of the creek of Béke Cave originates from the Aggtelek region. The Béke Cave is also part of the Aggtelek National Park and the UNESCO World Heritage. The cave was formed in the same Wetterstein Limestone as the Baradla Cave, its passages are also well decorated with big dripstones (mainly stalactites) and flowstones, but the corridors are smaller than in Baradla Cave (ca. 3-7 m wide and 10-15 m high). It is also mainly horizontal, with waterfalls 0.5-2.0 m in height. The tufa deposit (called „Nagytufa", abbreviated here as BNT) from which two drill cores were taken is approximately 100 m away from the artificial main entrance, the thickness of the overlying rock is about 45 m. The air temperature at the BNT site was 10.0 ±0.3 °C during the period of 2013-2015 (monthly measurements, n=58). The meteorological conditions at the surface are the same as for the Baradla Cave.

Csodabogyós Cave

N46°48´ E017°24´

Csodabogyós Cave is situated in Keszthely Mt, in western Hungary. The cave is a typical tectonic cave which has been formed in the 230 Ma old Ederics Limestone Formation. The cave entrance is located at an altitude of 393 m. The total length of surveyed passage is 5.2 km and the deepest chamber is located 121 m below the surface. The studied speleothem (CSB) was taken from the "Baldachin Chamber" which is located in 120 m from the cave entrance at a depth 30-35 m from the surface. Microclimate monitoring has been performed since 2012 in the "Baldachin Chamber" (Czuppon et al., 2014). Based on the three years of monthly measurements, the temperature is constant at 10.0±0.1 ˚C (i.e. shows no seasonality) at the studied site. The dripwater isotopic compositions are also stable, showing

no seasonal variations: δD=–71.9 ±1.1‰ and $\delta^{18}O$=–10.35 ±0.22‰. Based on data of nearby meteorological station at Keszthely (14 km W from the cave), the average annual air temperature varied between 9.1 and 11.6 ˚C in the period of 1996-2013 (the studied speleothem's formation commenced in 1996). The coldest months were January and February (from –0.6 to 1.0 ˚C) while the warmest are June, July and August (20.0 to 22.0˚C). The average annual precipitation is around 600 mm in the same period; the driest months are January and February (25-30 mm per month), while the wettest months are June to August (68 mm per month).

II. Descriptions and age constraints for the studied speleothems

Submillimeter thin alternating layers (dense and porous textures, dark and white in reflected light, translucent and opaque in transmitted light) were observed in the petrographic thin sections of the Csodabogyós and Baradla stalagmites (Figs. S1, S2). Both size and texture of these alternating laminae are in close resemblance to microsedimentological structure observed for seasonally alternating carbonate deposits in other European stalagmites (Baker et al., 2008; Mattey et al., 2008; Boch et al., 2011) and hence the dark-white lamina couplets were interpreted as annual increments. Independent information can verify in both caves the annual character of lamination in the studied speleothems.

Csodabogyós stalagmite

The actively growing CSB stalagmite was collected in 2013. The stalagmite was grown on a surface that was created in 1996 during cave exploration. Since stalagmite deposition may not start instantaneously after the new surface formation, the deposit can represent less than 17 years. The stalagmite's laminae are rather irregular with variable thickness (Fig S1a). Double-blind lamina counts by two researchers resulted 14 and 16 dark and white couplets (Fig. S1. b-c) which is in good agreement with the expected (<17) years of growth. Sample chips for coupled H-O isotope analyses were collected at a low resolution (2-5 mm). Deposition ages were estimated by simply partitioning the estimated total time of growth (15 years) proportionally to the distance from the surface.

Baradla, Nehézút stalagmites

The NU-1 and NU-2 stalagmites are 5 and 7 cm-tall; they were actively growing during their collection in 2013 and 2014, respectively. NU-1 is characterized by a more porous texture,

while NU-2 is well crystallized, however, both are characterized by fine (<1 mm) lamination (Fig. S2). Lamina counting on polished surfaces (Figs. S2a and d) yielded 47 and 155 laminae (dark and white couplets, Fig. S2) for NU-1 and NU-2, respectively. AMS radiocarbon analyses were performed on the NU-1 and NU-2 stalagmites in order to validate the annual character of the observed lamination. Samples were prepared following standard procedures (Molnár et al., 2011) and the $^{14}C/^{12}C$ and $^{13}C/^{12}C$ ratios were measured by the EnvironMICADAS ^{14}C facility in the Hertelendi Laboratory of Environmental Studies in Debrecen, Hungary (Molnár et al., 2013). Overall measurement uncertainty for a modern sample is <3‰, including normalization, background subtraction, and counting statistics. Activities are expressed in pMC (percent modern carbon).

^{14}C activity measurements on the NU-2 stalagmite were conducted in two runs. First a set of preliminary measurements was performed on samples drilled using a 3 mm-diameter drill bit in order to determine whether the so-called bomb peak is detectable in this particular sample. This pilot sampling was followed by a focused higher resolution re-sampling (ca. between 45 to 51 mm) using a 1 mm-diameter drill bit. The analyses revealed a ^{14}C activity rise up to 113.21±0.36 pMC (Table S1, and Fig. S3). The general notion is that any activity above 100 pMC is a clear indication of post-bomb atmospheric contribution (Baker et al., 2008). The peak itself can be tentatively placed at the center of the found plateau-like maximum of ^{14}C activities. Since this growth layer corresponds to the year 1967 obtained by lamina counting, a ~3 year shift can be assumed relative to the activity peak of 1964 in the corresponding atmospheric signal (NH1 Zone (Hua et al., 2013, Fig. S3b). This 3 year difference is a net effect of the transit time (infiltration delay) and the lamina counting error and can be regarded as a conservative error estimate for the lamina counting chronology. The largely dampened magnitude of the NU-2 ^{14}C record can be explained by the dead

carbon dilution and the contribution from aged soil carbon reservoir (Genty and Massault, 1999; Rudzka-Phillips et al., 2013).

The age estimation for the NU-1 stalagmite is supported by the ^{14}C activity measurements. The pMC values fall in the after-bomb range determined for the NU-2 stalagmite (*cf.* Table S1), indicating that the NU-1 stalagmite formation commenced some years after the 1964 bomb peak, which is in good agreement with the starting year of 1966 obtained by lamina counting (collection in 2013 – 47 laminae).

With the annual lamina formation proven by independent evidence, the ages of sampling points for geochemical analyses were estimated by proportional distance division (CSB), individual lamina identification (NU-1) and a polynomial age-depth model equation fitted to the lamina counting data for NU-2.

Béke Cave, Nagytufa deposit

The BNT-2 core (Fig. S4) was dated by means of U-Th method. Eight samples were cut from the core and dated (Shen et al., 2012; Cheng et al., 2013). Only four samples gave meaningful age dates with precisions better than ±500 years (Fig. S4b), whereas the other four samples were contaminated by detrital Th resulting in precisions between 1400 and 9200 years. The age date of 2 911 ± 1418 years BP is shown in Fig. S4b as it seems to fit the other data. Although the ages are not precisely constrained, we can conclude that the studied section of the core was formed in the last ca. 4000 years.

III. Analyses of liquid water samples and inclusion-hosted waters by laser spectroscopy

The laser spectroscope used in this study is a liquid water isotope analyser (LWIA) manufactured by Los Gatos Research Ltd, model LWIA-24d. Water samples were introduced into the spectroscope via an in-house designed vacuum line attached to the spectrometer (Czuppon et al., 2014). The analyses of liquid water samples were conducted following the procedure described earlier (Czuppon et al., 2014), whereas the method for inclusion water analysis was modified by connecting 4.6 grade He gas so that the sample tubes and the entire vacuum line could be flushed. Since the original method (Czuppon et al., 2014) was developed for the oxygen-free host mineral fluorite, the procedure applied for carbonate stalagmites is given in detail. Sample chips of several mm size were placed into the middle of 10 mm OD stainless steel tubes attached to the vacuum line using 6 mm-bore size Swagelok valves, and pumped for about 30 minutes to 10^{-3} mbar by means of a rotary pump and a liquid nitrogen cold trap. The vacuum line and samples were held at about 80 °C to remove the adsorptively bound water from the samples and the line. In order to avoid any thermal decrepitation of the inclusions and diffusion of H_2O out of the inclusions that may occur at 100 °C (Verheyden et al., 2008), the sample holder and samples were never heated to more than 85 °C. After vacuum pumping the sample and the vacuum line was continuously flushed with helium, maintaining pressure of several hundreds of mbar. Then the cold trap was immersed into liquid nitrogen and the tube containing sample was compressed while it was still hot (about 80 °C). Then the jaw of the press was removed and the tube was immediately heated to about 120 °C using a hot air gun and a temperature sensor attached to the sample tube. After about 3 minutes the helium flow was closed and the line was pumped to 10^{-3} mbar. Then the vacuum valve was closed and the H_2O collected from the stalagmite sample

was transferred to a liquid nitrogen-cooled cold finger connected to the spectroscope's inlet. The transfer of the sample takes place within 5 minutes, the usual vacuum reached 2-5 x 10^{-2} mbar. The non-condensable gases were pumped away. In order to reduce the effect of CO_2 collected together with water, the cold finger was immersed into ethanol cooled to about –80 °C. The pressure of the liberated CO_2 was recorded and subsequently pumped away. Then the extracted H_2O was let into the spectroscope and measured as for liquid water samples.

Measurement drifts, reproducibility and memory effect (van Geldern and Barth, 2012) were tested under different conditions by measuring δD and $\delta^{18}O$ values of three laboratory standard waters (BWS-1, 2, 3; Karman et al., 2014). The procedure developed for inclusion-hosted water was tested by injecting varying amounts of standard water into the vacuum line, frozen onto pre-heated calcite and then processed as water extracted from minerals. The results demonstrate (Czuppon et al., 2014) that this procedure did not cause appreciable changes in the measured compositions.

Measurements of laboratory standard waters selected for the same temperature conditions and corrected for the amount effect mentioned above generally resulted in reproducibilities better than ±0.5 and 0.1‰ for δD and $\delta^{18}O$ values, respectively (Czuppon et al., 2014). Since no internationally accepted standard exists for fluid inclusion analyses, the precision and accuracy can be demonstrated by analysing samples that had been investigated by conventional mass spectrometry and stalagmites where the dripwater compositions are known. Calcite samples already measured by TC/EA-IRMS were donated by Yuri Dublyansky (University of Innsbruck) and Hubert Vonhof (University of Amsterdam). Additionally, recently forming stalagmites were collected from the Baradla and the Csodabogyós Caves, where dripwater compositions have been monitored. The measured δD and $\delta^{18}O$ values are plotted as a function of expected compositions in Fig. S5. The δD values

plot along the 1:1 line and define a linear correlation with a slope of 0.95 (R^2=0.99), demonstrating the reliability of hydrogen isotope analysis. The $\delta^{18}O$ values plot parallel to the 1:1 line (with a slope of 0.99, R^2=0.97), but show a systematic shift of –0.88‰ from the expected values. It is important to note that the $\delta^{18}O$ shift from the expected value is larger for the Amsterdam samples than the average shift for the Innsbruck sample and for the recent stalagmites (-0.41‰). The $\delta^{18}O$ shift might be related to differences in instrumental set-up and analytical protocols. On the basis of the good fit to the Innsbruck sample and the dripwater compositions our data were corrected by +0.4‰.

Supplementary references

Baker, A., Smit, C.L., Jex, C., Fairchild, I.J., Genty, D., Fuller, L., 2008. Annually laminated speleothems: a review. International Journal of Speleology 37, 193–206.

Boch, R., Spötl, C., Frisia, S., 2011. Origin and palaeoenvironmental significance of lamination in stalagmites from Katerloch Cave, Austria. Sedimentology 58, 508–531.

Cheng H., Edwards R. L., Shen C.-C., Polyak V. J., Asmerom Y., Woodhead J., Hellstrom J., Wang Y., Kong X., Spötl C., 2013. Improvements in ^{230}Th dating, ^{230}Th and ^{234}U half-life values, and U-Th isotopic measurements by multi-collector inductively coupled plasma mass spectrometry. Earth and Planetary Science Letters 371-372, 82-91.

Czuppon, Gy., Kármán, K., Németh, S., Kiss, K., Demény, A., Szilárd, J., Kern, Z., Bíborka, M., Kohán, B., Haszpra, L., Siklósy, Z., 2014. Hydrogen and oxygen isotopic variation of cave drip waters: implications for recent climate and paleoclimate signal in stalagmite. In: Climate Change: The Karst Record (VII) KR7: 7th International Conference. Melbourne, Australia, p. 62–63.

Czuppon, Gy., Ramsay, R.R., Özgenc, I., Demény, A., Gwalani, L.G., Rogers, K., Eves, A., Papp, L., Palcsu, L., Berkesi, M., Downes, P.J., 2014. Stable (H, O, C) and noble-gas (He and Ar) isotopic compositions from calcite and fluorite in the Speewah Dome, Kimberley Region, Western Australia: implications for the conditions of crystallization and evidence for the influence of crustal-mantle fluid mixing. Minerogy and Petrology 108, 759-775.

Genty, D., Massault, M., 1999. Carbon transfer dynamics from bomb-^{14}C and δ^{13}C time series of a laminated stalagmite from SW France—modelling and comparison with other stalagmite records. Geochimica et Cosmochimica Acta 63,1537–1548.

Hiess, J., Condon, D.J., McLean, N., Noble, S.R., 2012. ^{238}U/^{235}U Systematics in Terrestrial Uranium-Bearing Minerals. Science 335, 1610-1614.

Hua, Q., Barbetti, M., Rakowski, A. Z., 2013. Atmospheric radiocarbon for the period 1950–2010. Radiocarbon 55, 2059–2072.

Jaffey, A.H., Flynn, K.F., Glendenin, L.E., Bentley, W.C., Essling, A.M., 1971. Precision measurement of half-lives and specific activities of ^{235}U and ^{238}U. Physical Review C 4, 1889–1906.

Karman, K., Maloszewski, P., Deak, J., Forizs, I., Szabo, C., 2014. Transit time determination for a riverbank filtration system using oxygen isotope data and the lumped-parameter model. Hydrological Sciences Journal 59, 1109-1116.

Mattey, D., Lowry, D., Duffet, J., Hodge, E., Frisia, S., 2008. A 53 year seasonally resolved oxygen and carbon isotope record from a modern Gibraltar speleothem: reconstructed dripwater and relationship to local precipitation. Earth and Planetary Science Letters 269, 80–95.

Molnár, M., Janovics, R., Major, I., Orsovszki, J., Gönczi, R., Veres, M., Leonard, A. G., Castle, S. M., Lange, T. E., Wacker, L., Hajdas, I., Jull, A. J. T., 2013. Status report of the new AMS C-14 sample preparation lab of the Hertelendi Laboratory of Environmental Studies, Debrecen, Hungary. Radiocarbon 55, 665–676.

Molnár, M., Rinyu, L., Veres, M., Seiler, M., Wacker, L., Synal, H.-A., 2013. EnvironMICADAS: a mini 14C-AMS with enhanced gas ion source interface in the Hertelendi Laboratory of Environmental Studies (HEKAL), Hungary. Radiocarbon 55, 338–344.

Rudzka-Phillips, D., McDermott, F., Jackson, A., Fleitmann, D., 2013. Inverse modelling of the ^{14}C bomb pulse in stalagmites to constrain the dynamics of soil carbon cycling at selected European cave sites. Geochimica et Cosmochimica Acta 112, 32–51.

Schen, C-C., Wu, C-C., Cheng, H., Lawrence Edwards, R., Hsieh, Y. T., Gallet, S., Chang, C.Chih, Li, T.Yong, Lam, D.Dinh, Kano, H., Hori, M., Spotl, C., 2012. High-precision and high-resolution carbonate ^{230}Th dating by MC-ICP-MS with SEM protocols. Geochimica et Cosmochimica Acta 99, 71-86.

van Geldern, R., Barth, J. A. C., 2012. Optimization of instrument setup and post-run corrections for oxygen and hydrogen stable isotope measurements of water by isotope ratio infrared spectroscopy (IRIS). Limnology and Oceanography: Methods 10, 1024–1036.

Verheyden, S., Genty, D., Cattani, O., van Breukelen, M. R., 2008. Water release patterns of heated speleothem calcite and hydrogen isotope composition of fluid inclusions. Chemical Geology 247, 266-281.

Figures

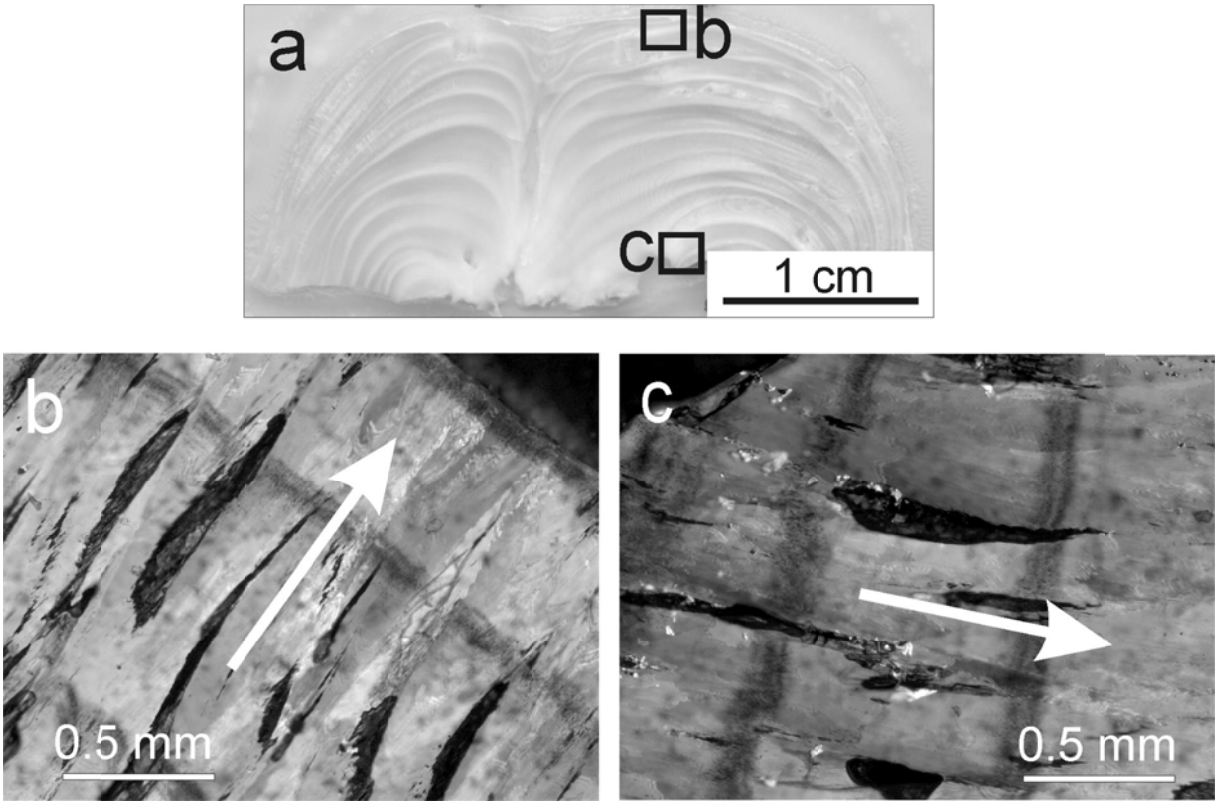

Fig. S1. Scanned picture of polished cross-section (a) and transmitted light optical microscopic pictures (b and c) taken with crossed Nicoles of the stalagmite of the Csodabogyós Cave. The approximate positions of the photos are marked in picture (a). Arrows show growth direction.

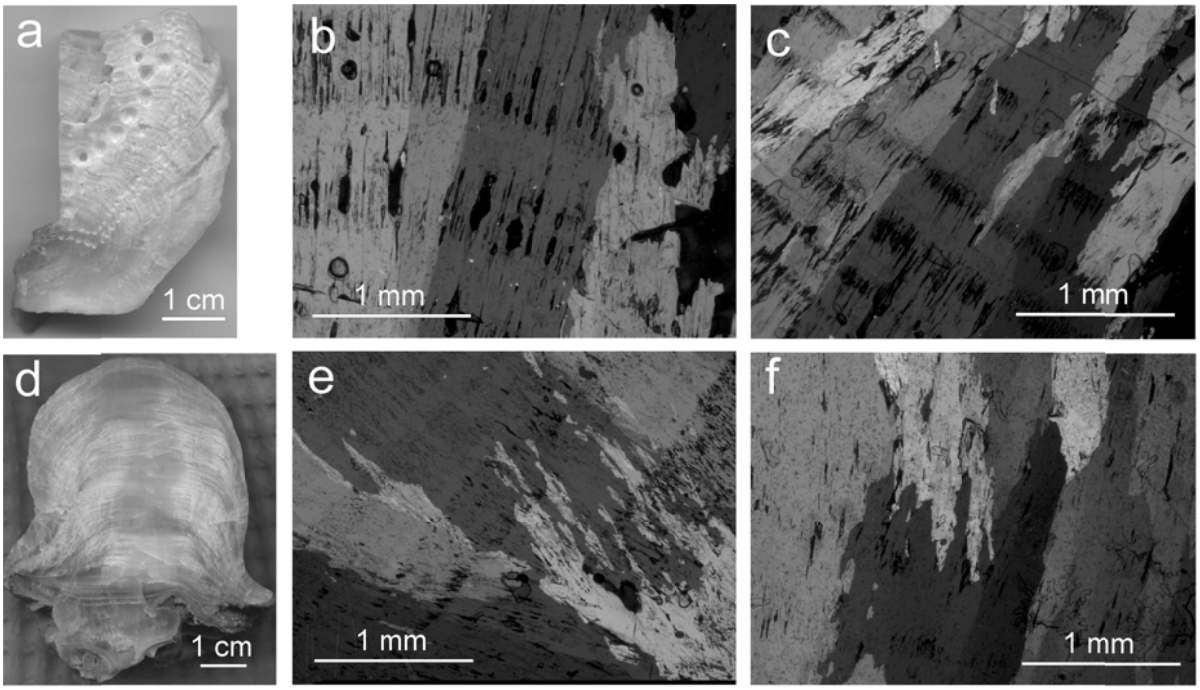

Fig. S2. Polished cross-sections (a: NU-1; d: NU-2) and optical microscopic pictures in transmitted light with crossed Nicols (b-c: NU-1; e-f: NU-2) of the N stalagmites from the Baradla Cave. Pictures (b) and (e) were taken close to the stalagmite top (youngest) parts, whereas pictures (c) and (f) were taken from parts closer to the base (oldest parts).

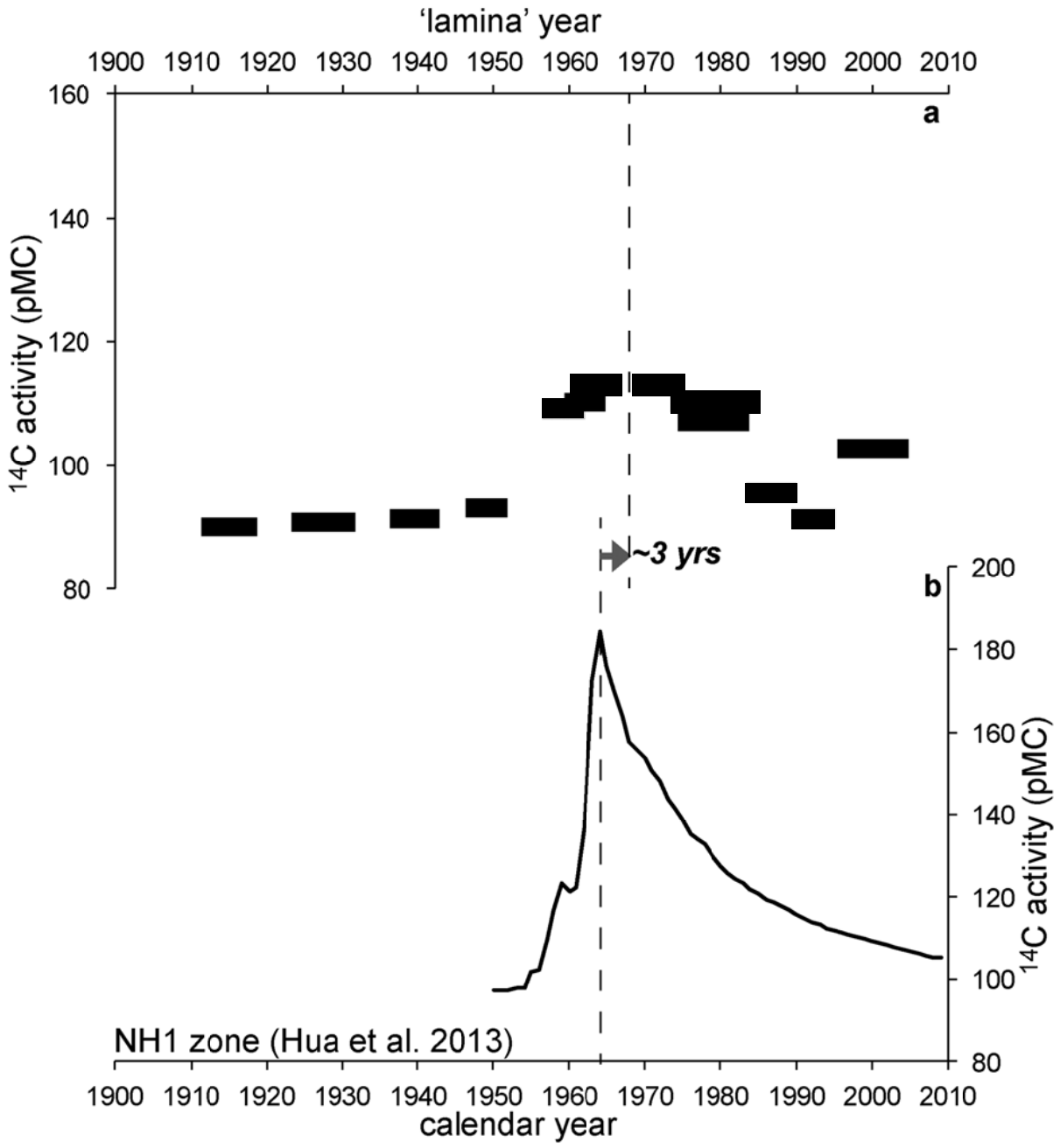

Fig. S3. ^{14}C activity values (plotted as black boxes representing sampling and measurement uncertainties) as a function of time for the NU-2 stalagmite (a) and the atmospheric signal (Hua et al., 2013) (b). The lag of ca. 3 years from the atmospheric signal is marked. Deposition time for NU-2 was obtained by lamina counting.

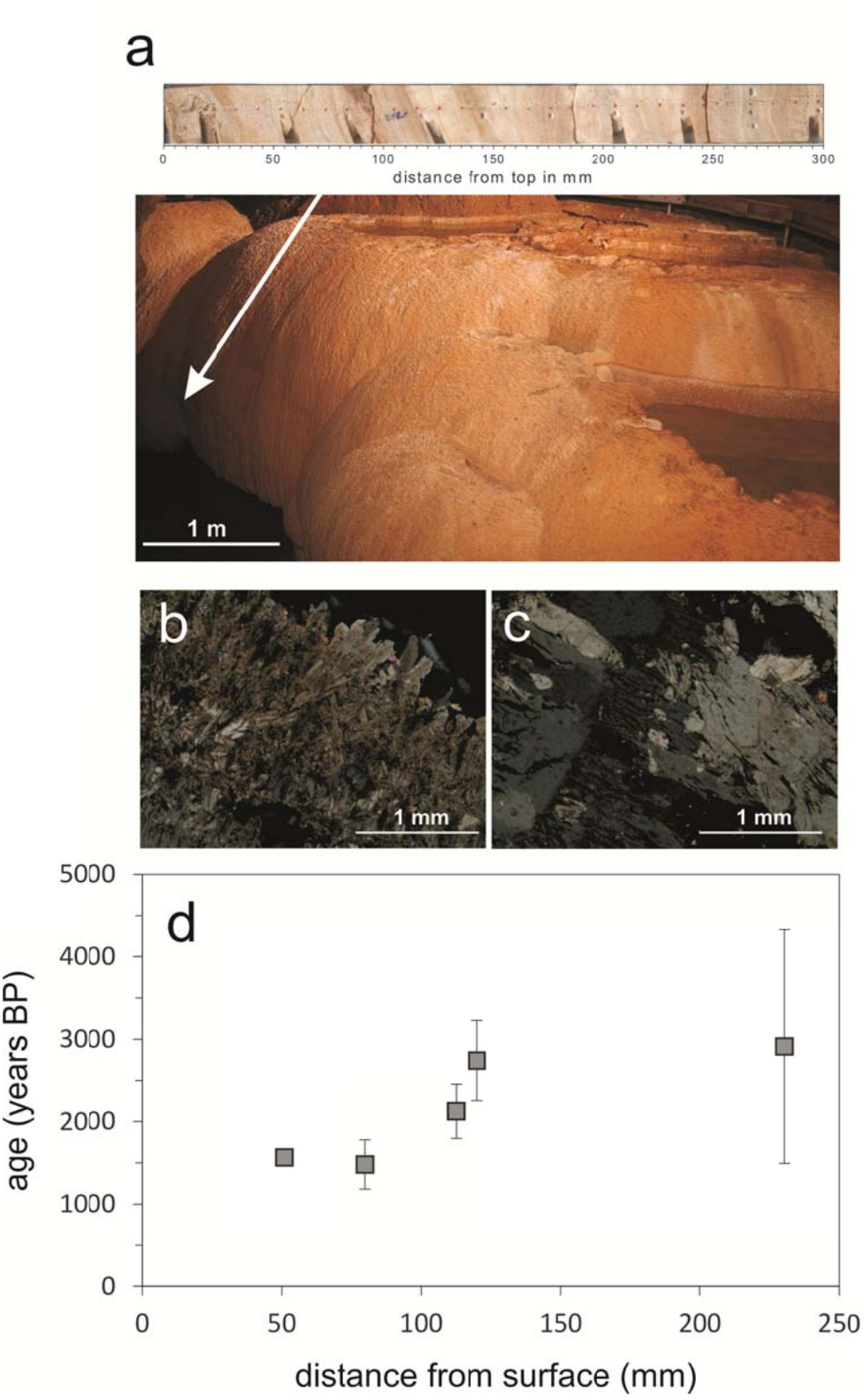

Fig. S4. Picture of the travertine terrace (a) formed in the Béke Cave and the polished cross-section of the drill core (sample BNT-2). Transmitted light microphotographs taken using

crossed Nicoles (b and c) of the BNT-2 cave-hosted travertine core showing dendritic calcite formed on the surface (b) and columnar calcite at 10 mm depth from surface (c). U/Th age dates (BP=Before Present) as a function of distance from the outermost surface of the BNT-2 drill core (d).

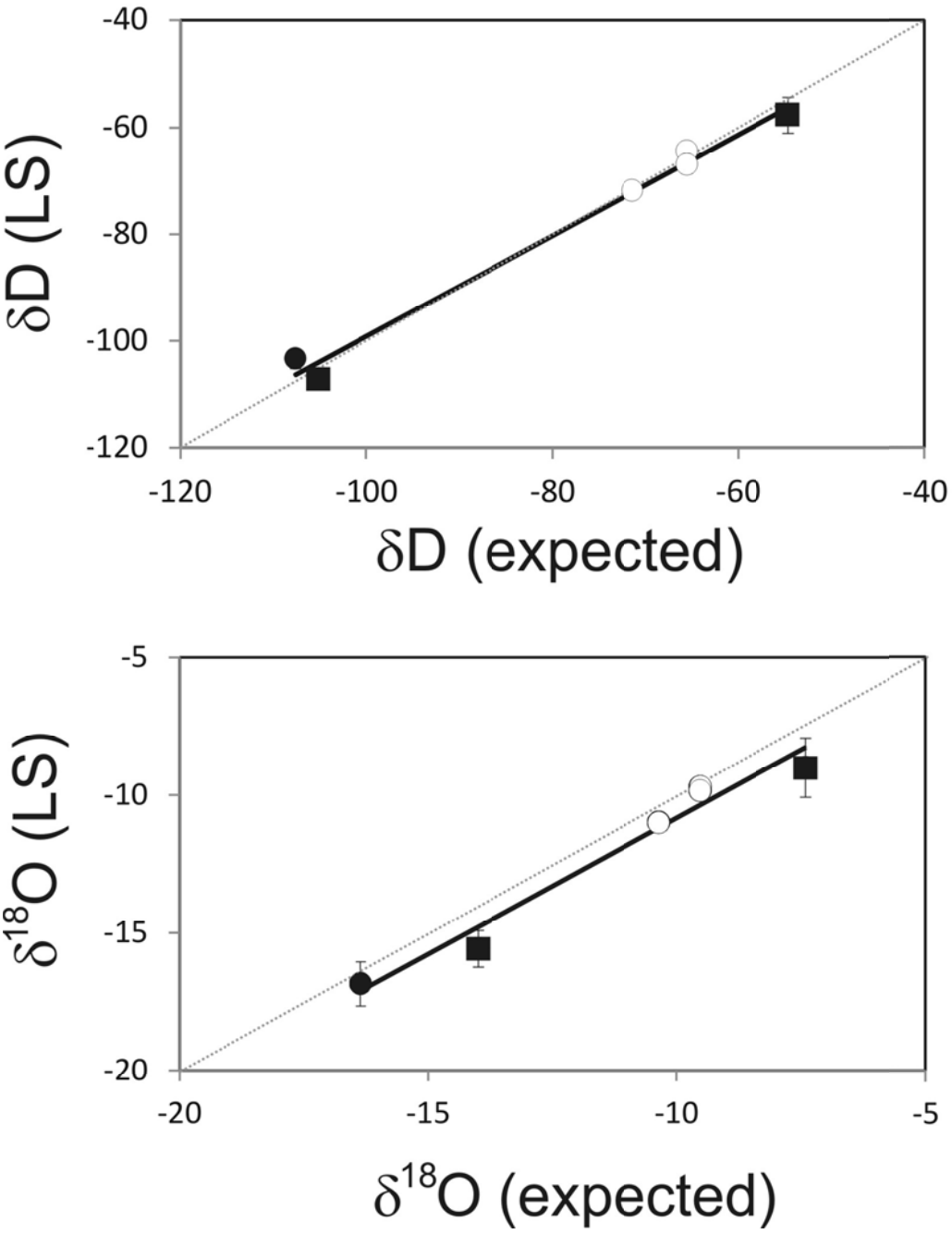

Fig. S5. Correspondence between H and O isotope compositions (in ‰ relative to V-SMOW) determined by laser spectroscopy (LS) and expected values (dripwater compositions at stalagmite sites [empty circles], values determined by isotopic-ratio mass spectrometry at the University of Innsbruck [filled circle] and at the University of Amsterdam [filled squares]).

Table S1. AMS ^{14}C analyses of the NU-1 and NU-2 stalagmites from the Baradla Cave, NE-Hungary. HEKAL is sample code at the Institute for Nuclear Research. Distance is in mm from the surface.

HEKAL	distance	pMC	±pMC	HEKAL	distance	pMC	±pMC
NU-1 stalagmite				*NU-2 stalagmite, preliminary analyses*			
I/798/1	1	99.33	0.42	I/936/1	2	102.70	0.32
I/798/2	5.5	98.42	0.41	I/936/2	5	107.02	0.29
I/798/3	10	99.70	0.41	I/936/3	8.5	110.21	0.31
I/798/4	14.5	98.86	0.41	I/936/4	12.7	93.04	0.27
I/798/5	19	100.41	0.41	I/936/5	16.5	91.30	0.25
I/798/6	23.5	98.65	0.40	I/936/6	19.7	90.75	0.27
I/798/7	28	98.89	0.41	I/936/7	23.1	90.01	0.25
I/798/8	32.5	100.32	0.41	I/936/9	30.5	91.96	0.26
I/798/9	37	100.45	0.41	I/936/10	33	92.47	0.28
I/798/10	41.5	101.32	0.41	*NU-2 stalagmite, high resolution analyses*			
I/798/11	46	101.09	0.41	I/965/1	5	91.49	0.28
I/798/12	50.5	100.87	0.42	I/965/2	6.9	95.72	0.29
				I/965/3	8.4	110.37	0.30
				I/965/4	9.8	113.21	0.36
				I/965/5	11	113.12	0.31
				I/965/6	12.5	109.23	0.34

Table S2. Uranium and Thorium isotopic compositions and U-Th ages for the BNT-2 travertine drill core measured by MC-ICPMS, Thermo Electron Neptune, National Taiwan University. Distance from the outer (recently forming) surface to the innermost (oldest) part of the core is given in cm in parentheses after sample ID number.

Sample ID (cm)	^{238}U ppb[a]		^{232}Th Ppt		$\delta^{234}U$ measured[a]		$[^{230}Th/^{238}U]$ activity[c]	
HD12 (51)	116.34	± 0.15	4.4	± 4.7	734.9	± 3.6	0.0247	± 0.0003
HD13 (80)	144.52	± 0.36	5266	± 48	737.1	± 8.2	0.0278	± 0.0017
HD14 (112.5)	82.51	± 0.18	3334	± 15	684.8	± 5.5	0.0373	± 0.0012
HD15 (120)	72.91	± 0.19	4597	± 23	752.9	± 6.6	0.0510	± 0.0018
HD16 (230.5)	82.82	± 0.19	15577	± 118	800.6	± 6.9	0.0697	± 0.0042

Sample ID (cm)	$[^{230}Th/^{232}Th]$ ppm[d]		Age uncorrected		Age corrected [c,e]		$\delta^{234}U_{initial}$ corrected[b]	
HD12 (51)	10768	± 11563	1 563	± 19	1 562	± 19	738.2	± 3.6
HD13 (80)	12.57	± 0.77	1 756	± 107	1 479	± 297	740.2	± 8.2
HD14 (112.5)	15.22	± 0.50	2 438	± 81	2 121	± 327	689.0	± 5.6
HD15 (120)	13.35	± 0.47	3 216	± 114	2 741	± 489	758.7	± 6.8
HD16 (230.5)	6.11	± 0.37	4 295	± 263	2 911	± 1418	807.2	± 7.7

Analytical errors are 2σ of the mean.

[a] $[^{238}U] = [^{235}U] \times 137.818$ (±0.65‰) (Hiess et al., 2012), $\delta^{234}U = ([^{234}U/^{238}U]_{activity} - 1) \times 1000$.

[b] $\delta^{234}U_{initial}$ corrected was calculated based on ^{230}Th age (T), i.e., $\delta^{234}U_{initial} = \delta^{234}U \, X \, e^{\lambda_{234}*T}$, and T is corrected age.

[c] $[^{230}Th/^{238}U]_{activity} = 1 - e^{-\lambda_{230}T} + (\delta^{234}U/1000)[\lambda_{230}/(\lambda_{230} - \lambda_{234})](1 - e^{-(\lambda_{230} - \lambda_{234})T})$, where *T* is the age.

Decay constants are 9.1705×10^{-6} yr^{-1} for ^{230}Th, 2.8221×10^{-6} yr^{-1} for ^{234}U (Cheng et al., 2013), and 1.55125×10^{-10} yr^{-1} for ^{238}U (Jaffey et al., 1971).

[d] The degree of detrital ^{230}Th contamination is indicated by the $[^{230}Th/^{232}Th]$ atomic ratio instead of the activity ratio.

[e] Age corrections for samples were calculated using an estimated atomic $^{230}Th/^{232}Th$ ratio of 2 ± 2 ppm, estimated with active deposition.

Table S3. Chemical compositions (in ppm) of the studied speleothems determined by ICP-MS analyses at the Eötvös Loránd University. Analytical details and discussions are given in the main text. Distances are in mm from the outermost sample surface.

	distance	Mg	Sr	Si	Al	Fe		distance	Mg	Sr	Si	Al	Fe
NU-1	2.5	127	31	2	9	37	**CSB**	1	2817	47	123	84	39
	4.5	120	30	5	7	29		5.1	2608	53	122	30	18
	7	112	31	5	4	12							
	8.75	134	31	2	4	15	**BNT-2**	20	587	25	3505	1411	1070
	11	130	32	6	3	19		50	370	23	nd	39	19
	13	134	34	9	4	13		80	338	32	38	27	17
	15	128	34	9	7	17		110	350	18	nd	67	34
	18	132	36	14	6	6		140	433	18	nd	77	166
	22.5	146	30	75	11	37		170	327	25	nd	134	nd
	24.5	107	37	19	4	2		200	344	19	nd	nd	nd
	26.5	121	34	32	5	5		230	346	23	nd	40	16
	28.25	114	41	33	6	9		260	354	24	1010	700	406
	30.5	126	31	50	10	2983		290	265	29	426	362	149
								310	281	28	623	509	277
NU-2	0.5	476	74	22	2	6		340	274	33	631	524	274
	4.8	388	58	24	7	5		370	230	31	305	285	108
	8.9	378	63	22	7	4		400	242	32	220	242	92
	14.45	404	72	28	18	11		430	269	29	281	272	196
	18.8	339	62	23	7	3		460	332	39	462	395	334
	22.95	312	50	26	5	5		490	206	26	56	86	65
	26.8	328	70	30	24	24							
	31	353	64	32	2	2							
	35.85	376	48	24	6	3							
	39.25	355	46	25	5	3							
	41.85	331	41	21	24	14							
	46.4	350	41	55	70	65							
	50.95	337	60	25	4	5							
	55.6	354	61	38	14	19							
	58.7	396	53	27	47	45							

Table S4. XRD data obtained from spectra (see main text). Sample numbers are for the XRD analyses. Distance is in mm from surface. FWHM: full width at half-maximum.

sample	distance	FWHM	D(Å)	sample	distance	FWHM	D(Å)
CSB-1	1	0.158	559	BNT-2/f	2	0.140	632
CSB-2	2	0.146	604	BNT-2/1	22	0.144	613
CSB-3	3.6	0.152	579	BNT-2/4	43	0.139	637
CSB-4	4.2	0.144	618	BNT-2/5	48	0.136	652
CSB-5	5.1	0.161	548	BNT-2/21	132	0.122	734
CSB-6	6.9	0.145	609	BNT-2/22	137	0.129	691
CSB-7	12.7	0.145	609	BNT-2/23	142.5	0.125	715
NU-1/1	2	0.140	632	BNT-2/25	152	0.132	674
NU-1/2	7.5	0.126	709	BNT-2/26	156	0.129	691
NU-1/3	22	0.123	727	BNT-2/28	165.5	0.126	709
NU-1/4	30	0.127	702	BNT-2/30	176.5	0.123	727
NU-1/5	45	0.121	740	BNT-2/31	182.5	0.131	679
NU-2/1	2	0.159	552				
NU-2/2	8	0.138	642				
NU-2/3	14	0.136	652				
NU-2/4	20	0.126	709				
NU-2/5	26	0.121	741				

Table S5. Stable hydrogen and oxygen isotope compositions of inclusion-hosted water from speleothems (travertine deposit and stalagmites) and dripwaters of the deposits' sites. The isotope values are reported in ‰ relative to V-SMOW.

sample	distance	δD	$\delta^{18}O$	sample	distance	δD	$\delta^{18}O$
Travertine core BNT-2				*Stalagmite NU-1*			
FL BNT-2/1	10	-62.1	-9.1	FL NU-1/1	3	-67.2	-9.3
FL BNT-2/2	42	-66.8	-9.5	FL NU-1/2	7	-67.7	-12.7
FL BNT-2/3	43	-70.0	-11.0	FL NU-1/3	12	-71.0	-11.5
FL BNT-2/4	45	-63.2	-10.3	FL NU-1/4	21	-66.3	-11.7
FL BNT-2/5	48	-75.8	-13.1	FL NU-1/5	23	-70.6	-12.7
FL BNT-2/6	52	-69.0	-10.7	FL NU-1/6	26	-65.3	-12.7
FL BNT-2/7	56	-71.8	-11.2	FL NU-1/7	34	-68.9	-13.0
FL BNT-2/8	140	-65.7	-13.8	FL NU-1/8	44	-68.7	-11.7
FL BNT-2/9	142.5	-70.3	-12.9				
FL BNT-2/10	150	-65.4	-14.3	*Stalagmite NU-2*			
FL BNT-2/11	154	-61.4	-11.9	FL NU-2/1	2.5	-65.9	-10.0
FL BNT-2/12	160.5	-65.1	-12.9	FL NU-2/2	5	-63.6	-9.1
FL BNT-2/13	165.5	-70.7	-14.1	FL NU-2/3	7.5	-62.8	-8.9
FL BNT-2/14	170.5	-67.2	-11.4	FL NU-2/4	8	-65.8	-10.4
FL BNT-2/15	175	-62.4	-13.1	FL NU-2/5	17	-68.9	-11.3
FL BNT-2/16	176.5	-72.7	-13.0	FL NU-2/6	22	-65.4	-11.0
FL BNT-2/17	182.5	-63.7	-10.9	FL NU-2/7	29	-66.8	-10.1
FL BNT-2/18	183	-61.9	-11.6	FL NU-2/8	36.5	-63.5	-9.2
FL BNT-2/19	189	-68.5	-14.7	FL NU-2/9	42.5	-63.5	-9.1
FL BNT-2/20	189	-70.1	-11.9	FL NU-2/10	49	-65.2	-9.6
FL BNT-2/21	195	-67.1	-12.1	FL NU-2/11	50	-65.1	-9.8
FL BNT-2/22	201	-65.2	-13.1				
FL BNT-2/23	207	-68.4	-12.5	*Stalagmite CSB*			
FL BNT-2/24	213	-65.8	-14.2	FL CSB-1	10	-71.5	-11.8
FL BNT-2/25	219	-66.4	-13.3	FL CSB 2	3	-72.9	-10.6
FL BNT-2/26	225	-69.6	-14.5				
FL BNT-2/27	231	-65.0	-10.7	NU dripwater		-66.2	-9.5
FL BNT-2/28	237	-68.7	-12.6	CSB dripwater		-71.9	-10.4
FL BNT-2/29	249	-68.8	-13.4	BNT dripwater		-66.3	-9.5